

# Atomic Scale Measurement of Polar Entropy

Debangshu Mukherjee,<sup>1</sup> Sergei Prokhorenko,<sup>2,3</sup> Leixin Miao,<sup>1</sup> Ke Wang,<sup>4</sup> Eric Bousquet,<sup>2</sup> Venkatraman Gopalan,<sup>1,4</sup> and Nasim Alem<sup>1,4,\*</sup>

<sup>1</sup>*Department of Materials Science and Engineering, The Pennsylvania State University, University Park, Pennsylvania 16802, USA*

<sup>2</sup>*Theoretical Materials Physics Q-MAT CESAM, University of Liège, Sart Tilman B-4000, Belgium*

<sup>3</sup>*Physics Department and Institute for Nanoscience and Engineering, University of Arkansas, Fayetteville, Arkansas 72701, USA*

<sup>4</sup>*Materials Characterization Laboratory, Materials Research Institute, The Pennsylvania State University, University Park, Pennsylvania 16802, USA*

Entropy is a fundamental thermodynamic quantity that is a measure of the accessible microstates available to a system<sup>1</sup>, with the stability of a system determined by the magnitude of the total entropy of the system. This is valid across truly mind boggling length scales - from nanoparticles to galaxies<sup>2,3</sup>. However, quantitative measurements of entropy change using calorimetry are predominantly macroscopic, with direct atomic scale measurements being exceedingly rare<sup>4</sup>. Here for the first time, we experimentally quantify the polar configurational entropy (in meV/K) using sub-ångström resolution aberration corrected scanning transmission electron microscopy. This is performed in a single crystal of the prototypical ferroelectric LiNbO<sub>3</sub> through the quantification of the niobium and oxygen atom column deviations from their paraelectric positions. Significant excursions of the niobium–oxygen polar displacement away from its symmetry constrained direction is seen in single domain regions which increases in the proximity of domain walls. Combined with first principles theory plus mean field effective Hamiltonian methods, we demonstrate the variability in the polar order parameter, which is stabilized by an increase in the magnitude of the configurational entropy. This study presents a powerful tool to quantify entropy from atomic displacements and demonstrates its dominant role in local symmetry breaking at finite temperatures in classic, nominally Ising ferroelectrics.

PACS numbers: 65.40.gd, 68.37.Ma, 77.80.Dj, 77.84.Ek

Keywords: LiNbO<sub>3</sub>, Ferroelectricity, Domain Wall, Polar Entropy, Aberration Corrected STEM

## I. INTRODUCTION

While absolute entropy, a fundamental thermodynamic parameter, is difficult to experimentally measure macroscopically, a change in entropy ( $\Delta S = \Delta Q_{\text{rev}}/T$ ), is usually measured using calorimetry, where  $\Delta Q_{\text{rev}}$  is the reversible heat supplied to the system at a constant temperature  $T$ <sup>1,4</sup>. At absolute zero ( $T = 0\text{K}$ ), the total entropy of a perfect crystal free of dopants is zero. Upon addition of reversible heat to the system, the entropy increases. Directly measuring the absolute entropy of the system through characterizing the microscopic configurations, or the microstates, is challenging, since it increases exponentially with the number of available microstates. Such enormously large numbers of microstates are also involved in condensed matter systems where a dopant atom may choose any one of equivalent atomic sites in a periodic lattice. The perturbation in atom positions from the crystal sites thus leads to an increase in the configurational entropy - which can be quantified through the probability distributions of the perturbations. Such configurational entropy may arise for example in ferroelectric crystals - due to perturbations in the order parameter. The order parameter of a ferroelectric system is the spontaneous polarization, which arises as a consequence of the polar displacements<sup>5</sup>. The advances in aberration corrected scanning transmission electron microscopy (STEM) - have now made it possible to quantify displacements with a precision approaching a single picometer<sup>6–8</sup>, and even below a single picometer<sup>9</sup>. Recent results have demonstrated the feasibility

of visualizing 2pm magnitude charge density waves even at cryogenic temperatures with dark field STEM<sup>10</sup>. We build upon these advances to perform picometer precision quantification of polar displacements to quantify the variation in the order parameter in the well-known optical ferroelectric LiNbO<sub>3</sub> relative to its' ideal ferroelectric structure. Throughout the rest of this work, we will refer to this entropy arising from the variability in polar displacements as polar entropy.

## II. MEASUREMENT OF NIOBIUM–OXYGEN POLAR DISPLACEMENTS

Ferroelectric materials have a spontaneous and switchable electrical polarization, which is a consequence of the lattice distortions in the crystal structure that break inversion symmetry<sup>11</sup>. Regions of uniform polarization are called domains, with the boundary between two adjacent domains referred to as a domain wall<sup>12,13</sup>. Since the ferroelectric polarization is a consequence of crystal lattice distortions, the possible polar vectors can occur only along certain symmetry allowed crystallographic directions. As a uniaxial displacive ferroelectric (space group R3c), the origin of the spontaneous polarization in LiNbO<sub>3</sub> is a consequence of the niobium and lithium cation displacements with respect to the oxygen octahedral center along either the (0001) or the (000 $\bar{1}$ ) crystallographic axes, and thus the polarization vectors are restricted to only (0001) direction (also labeled as z- or 3- direction)<sup>14</sup>. Classical uniaxial ferroelectrics such as LiNbO<sub>3</sub> have been long thought of as Ising like where the

polarization is only along the two symmetry restricted directions, which transitions to zero at the domain wall, since lattice distortions away from the symmetry restricted polarization directions have a high energy cost associated with them<sup>15,16</sup>. However, recent research have pointed out that fluctuations away from the Ising polarization direction do exist in other ferroelectrics - most notably  $\text{PbTiO}_3$ , with Bloch and Néel components arising at domain walls<sup>17-20</sup>. However, such deviations, as per the authors' knowledge have never been observed before in  $\text{LiNbO}_3$ .

To visualize the atom positions at the  $180^\circ$  domain wall and also at the bulk domain, we imaged the electron transparent  $\text{LiNbO}_3$  sample from the  $[1\bar{1}00]$  crystallographic zone axis so that the Ising displacements lie in plane. While both bright field (BF) and annular dark field (ADF) STEM images were acquired (Figure 1(a) and Figure 1(b)), we exclusively use BF-STEM images for the quantification of polar displacements since both the niobium and oxygen atom positions and their relative displacements can be quantified. This technique has been previously demonstrated as a viable pathway for the determination of the cation and oxygen atom positions simultaneously<sup>21</sup>, and is less susceptible to specimen tilt and defocus in comparison to annular bright field (ABF)-STEM<sup>22,23</sup>. The samples imaged in this experiment were approximately 25nm thick, as determined from electron energy loss spectroscopy (EELS) inelastic mean free path measurements (see Figure 7 in appendix)<sup>24</sup>.

The total polar displacements are calculated per unit cell, with respect to a mean unit cell calculated from the entire image (Figure 1(c)). The mean unit cell calculated from the STEM experimental data has the dimensions of  $1390\text{pm} \times 259\text{pm}$  - which is within 2% of the simulated  $\text{LiNbO}_3$   $R3c$  unit cell parameters of  $1412.92\text{pm} \times 261.15\text{pm}$  when viewed from the  $[1\bar{1}00]$  crystallographic zone axis<sup>25</sup>. As demonstrated in Figure 1(d), displacements along  $\langle 0001 \rangle$  are the Ising displacements, while those along  $\langle 11\bar{2}0 \rangle$  are the Néel displacements. To determine the polar displacements, we first assigned the measured atom positions to their corresponding  $\text{LiNbO}_3$  unit cell positions, and then generated an average unit cell by summing all the individual unit cells throughout the BF-STEM image (Figure 1(d)). The oxygen and niobium centers of mass for each individual unit cell (Figure 1(e)) were subsequently compared to the center of the calculated mean unit cell to determine the displacement vectors for both niobium and oxygen atoms for each  $\text{LiNbO}_3$  unit cell imaged. The Nb-O polar displacement were then measured as a vector subtraction of the oxygen displacement vector from the niobium displacement vector. This calculated polar displacement vector was subsequently decomposed into its corresponding Ising and Néel components along the  $\langle 0001 \rangle$  and  $\langle 11\bar{2}0 \rangle$  directions respectively to obtain the individual polar components.

### III. POLAR DISPLACEMENTS AT THE BULK DOMAIN AND THE DOMAIN WALL

Figure 2(a) demonstrates a section of the domain wall, with the scaled Ising displacements overlaid on the corresponding BF-STEM image. The blue regions refer to Ising displacements along  $[000\bar{1}]$  axis, while the red regions indicate the Ising displacements along the  $[0001]$  direction. The  $180^\circ$  nature of the wall and the domain reversal across only one to two unit cells could be immediately ascertained, with the displacements being associated with simultaneous motion of both the niobium and the oxygen centers. Our measurements point to both oxygen and niobium atom columns displacing across the wall giving rise to a combined Ising displacement of 55 pm across the  $180^\circ$  domain wall as demonstrated in Figure 2(a). Similar values for niobium displacements ( $\approx 25\text{pm}$ ) have been recently reported in  $\text{LiNbO}_3$  through tracking the niobium atom columns with ADF-STEM<sup>26</sup>. In addition, the wall does not maintain a sharp atomic structure showing kinks and bends along itself as shown in Figure 2(a). Figure 2(b) demonstrates that the domain wall and its proximity are also characterized by regions of Néel displacements, with parts of the wall featuring higher Néel intensities compared to the neighboring domain. In contrast to the Ising displacements, which are driven by the cooperative motion of oxygen and niobium atoms across the domain wall, the Néel displacements are however primarily driven by the niobium atoms reaching a maxima in absolute magnitude at the wall. We observe also that while the absolute magnitude of Néel displacements increase at the domain wall, Figure 2(b) shows non-zero Néel displacements even inside the domain. Such non-Ising displacements have been predicted before at domain wall, though one may not expect them in a hard uniaxial ferroelectric<sup>27</sup>. Additionally, we observe that the maxima of the Néel displacements are not collocated with the center of the Ising displacements - as can be observed from Figure 2(d). This offset is due to the fact that the wall is not straight as indicated in Figure 2(a-b). While the middle of the wall shows stronger Néel components, in the top half of the wall the Néel displacements die out due to the slight bending of the wall.

From the Ising and Néel displacements which we map in Figure 2(a) and Figure 2(b) respectively, it is obvious that contrary to the classical expectation of a pure Ising wall, non-Ising displacements do in fact occur. This is apparent as the magnitude of the curl increases at the wall (Figure 2(c)), indicating clockwise rotation of the polar Niobium-Oxygen displacement vectors. The Néel displacements however at the domain wall have a directional preference, which may be due to the higher electrostatic energy needed for head-to-head or tail-to-tail configurations arising from bidirectional Néel displacements. The electron microscope thus paints a picture of the  $180^\circ$   $\text{LiNbO}_3$  domain wall where the polar displacements demonstrate variation spatially, something that we observed consistently at other images of the domain wall too (Figure 15, Figure 16, Figure 17 and Figure 18), and even in images of the bulk domain (Figure 13 and Figure 14), indicating perturbations in the polar order parameter, and

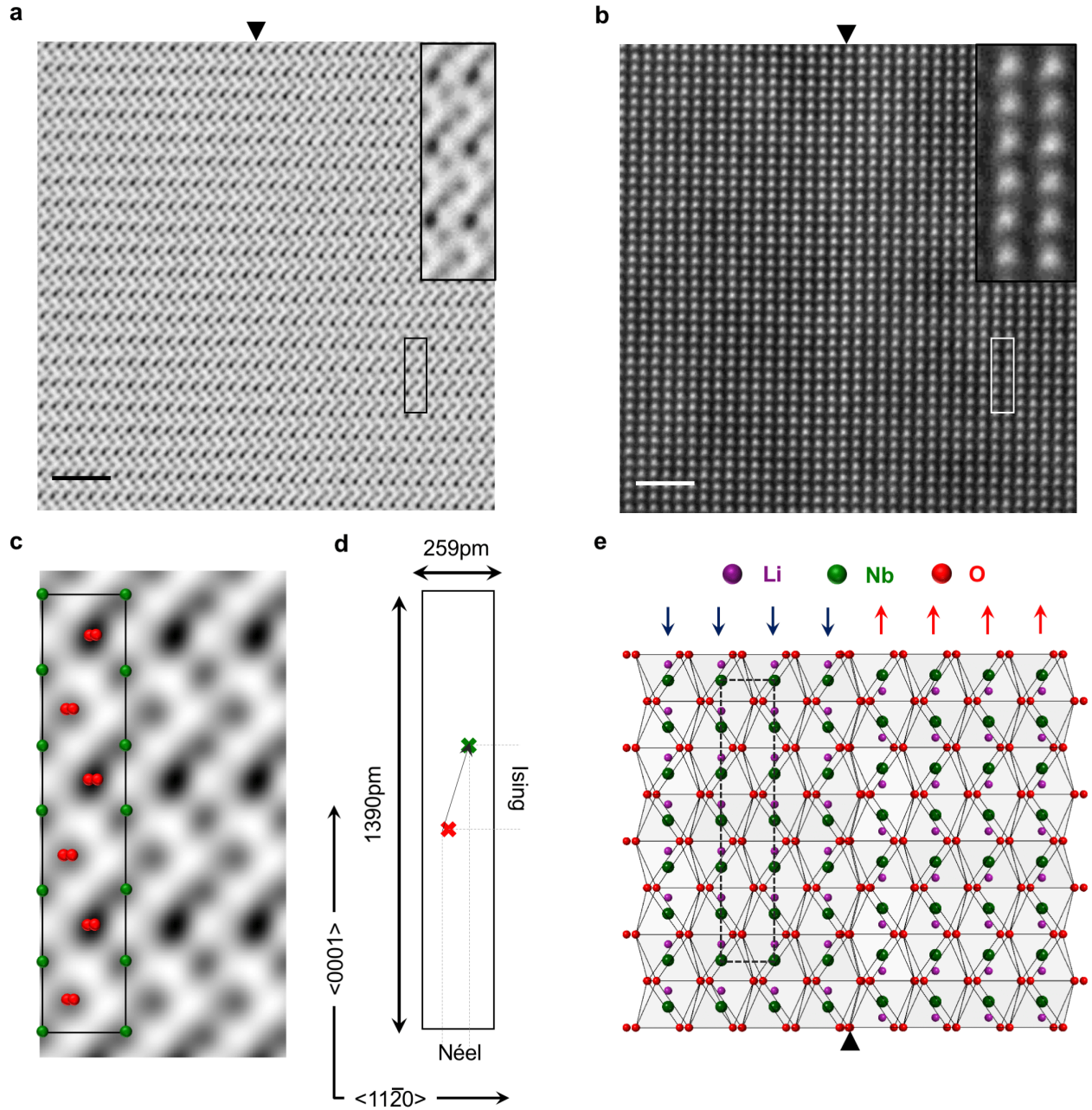


FIG. 1. Schematic of electron microscopy experiments. (a) Aberration-corrected Bright Field (BF)-STEM image of a domain wall in  $\text{LiNbO}_3$ , with the wall location marked by the black triangle, with a zoomed section in inset showing oxygen and niobium positions. Scale bar is 2nm. (b) Simultaneously collected Annular Dark Field (ADF)-STEM image of the region imaged in Figure 1(a), with the wall location marked by the black triangle. The zoomed section in inset shows the niobium atoms. Scale bar is 2nm. (c) Averaged mean unit cell from the experimental datasets with the niobium positions in green and the oxygen atoms in red. The unit cell is shown as the black rectangle. (d) The schematic of the unit cell with the experimentally measured long and short dimensions. The niobium and oxygen centers are shown as green and red crosses with the projected Ising and Néel displacement directions. (e) Atomic model of  $\text{LiNbO}_3$  crystal structure viewed from the  $[1\bar{1}00]$  zone axis, with lithium atoms in purple, niobium atoms in green and oxygen atoms in red. The average unit cell for polarization calculations is shown as a black dashed box with the arrows referring to the polarization direction.

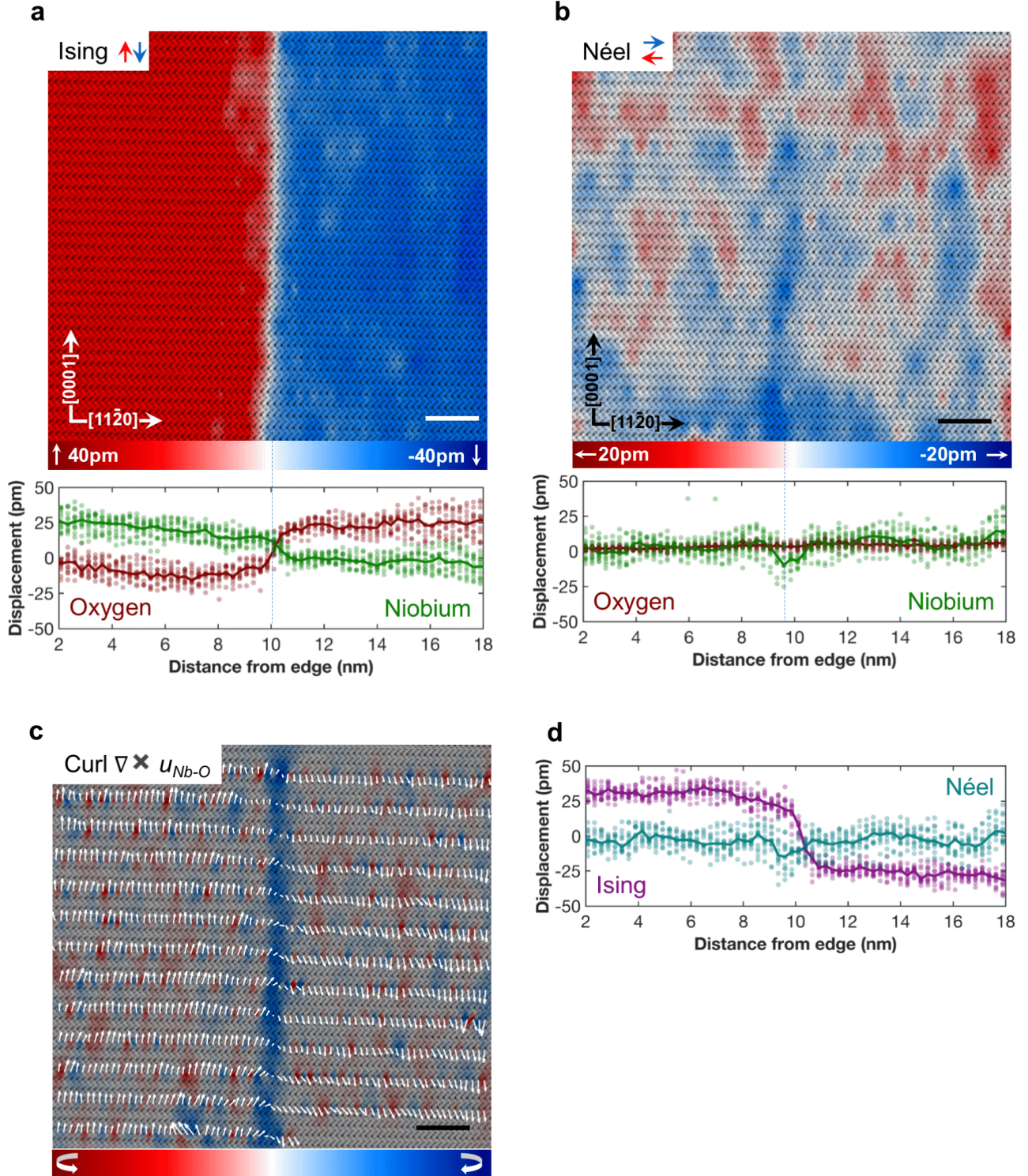


FIG. 2. Polar displacements measured with BF-STEM. (a) LiNbO<sub>3</sub> domain wall imaged from  $[1\bar{1}00]$  zone axis with the polar Ising niobium-oxygen displacements overlaid. Scale bar is 2 nm. The Ising niobium and oxygen along the  $\langle 0001 \rangle$  direction in green and red respectively with the solid lines referring to the averages are plotted below. (b) Polar niobium-oxygen Néel displacements overlaid on the BF-STEM image. Scale bar is 2 nm. The Néel niobium and oxygen along the  $\langle 11\bar{2}0 \rangle$  direction in green and red respectively with the solid lines referring to the averages are plotted below. (c) Curl of the niobium-oxygen displacement vector overlaid on the BF-STEM image, with the rotation vectors overlaid in white. (d) Niobium and oxygen relative Ising and Néel displacements.

thus increased polar entropy at the wall.

To visualize the polar behavior away from the domain wall, we also imaged a section of the bulk domain, approximately 100nm away from the domain wall in Figure 3(a - b). As expected, the Ising displacement direction and magnitude does not change in the bulk domain, in contrast to the Ising displacements right across the domain wall (Figure 3(c)). Additionally we observe Néel displacements both in the bulk domain (Figure 3(b)) and at the domain wall (Figure 3(d)), with visual inspection confirming lower absolute magnitudes in the bulk domain. To understand the variability of the polar niobium–oxygen displacements at the domain wall with respect to the domain, we calculated the absolute magnitude of the Ising and Néel displacements in Figure 3(e). These measurements demonstrate the Néel displacements reaching values below 5 pm at distances over 100 nm away from the wall, but they do not completely die down. In contrast, the absolute magnitude of the Néel displacements increases in the proximity of the domain wall – along with a significantly higher spread in displacement magnitudes of both Ising and Néel displacements at the domain wall compared to the bulk domain. It should be noted that both the images were obtained from the same TEM sample, and with the same exact imaging conditions. While microscope mechanical vibrations, sample preparation effects and inhomogeneities in the chemical and atomic structure can locally induce random fluctuations, this long-range decrease in the magnitude of Néel displacements (at the domain wall as opposed to the bulk domain) are probably intrinsic to  $\text{LiNbO}_3$  itself, originating from polar instabilities at the domain wall.

#### IV. FIRST PRINCIPLES CALCULATIONS OF DISPLACEMENT ENERGETICS

To understand the origin of the observed polar instabilities, we performed DFT calculations of phonons in the high symmetry phase of  $\text{LiNbO}_3$ . In agreement with previous calculations we observed three unstable modes at the  $\Gamma$  point -  $A_{2u}$  and  $E_u$  polar modes with polarization parallel and perpendicular to the  $[0001]$  direction respectively and the  $A_{2g}$  Raman mode (see Figure 12 and Table II)<sup>28</sup>. The polar  $A_{2u}$  mode has a significant overlap with the vector representing the atomic displacements during the phase transition and therefore describes the displacement pattern responsible for the Ising macroscopic polarization of the ground state ferroelectric phase of  $\text{LiNbO}_3$ .

Moreover, we observe that the polar displacements along the Néel/Bloch direction (associated with the doubly degenerate  $E_u$  mode), are unstable and the system can thus lower its energy with polar displacements perpendicular to the  $[0001]$  Ising direction. This can explain our experimental results, i.e. the presence of Néel and Bloch polarization directions at the domain wall where the Ising polarization amplitude is strongly reduced along the Ising direction. Besides that, within a bulk ferroelectric domain, the  $E_u$  mode instability is suppressed by the  $A_{2u}$  mode condensation and the associated strain relaxation, however the energy land-

scape is still sufficiently shallow to allow deviations of local dipole directions from the Ising  $(0001)$  axis. Thus while the  $A_{2u}$  mode is the dominant mode driving ferroelectricity, the instability from the  $E_u$  modes makes it energetically favorable for the non-Ising fluctuations to arise from the ideal  $\text{LiNbO}_3$  polar configuration, thus increasing disorder in the system.

The resultant energy landscape related to the displacements of atoms strictly perpendicular to the  $(0001)$  Ising axis ( $E_u$  mode) complies with  $SU(1)$  unitary group rotation symmetry resulting in the famous Goldstone sombrero potential shape with zero Ising component (Figure 4(a)). The suppression of the Ising displacements in the  $(0001)$  direction thus leads to a spontaneous symmetry breakdown giving rise to the perpendicular Néel and Bloch components, with the radial magnitude of the perpendicular components reaching an energy minima at 8pm displacement (Figure 4(b)). We also note that the experimentally observed Néel magnitudes of approximately 10pm at the domain wall (Figure 2(d)) are close to the theoretically predicted displacement magnitude at the energy minima. Note however that these experiments cannot quantify the predicted Bloch displacements, because transmission electron microscopy probes a two-dimensional projection of columns of atoms, and Bloch displacements would be parallel to the atomic columns. Thus it was not possible to determine whether the magnitude of the non-Ising polar components stayed constant (massless Goldstone modes) or varied across the domain boundary (massive Higgs modes)<sup>29,30</sup>. These calculations demonstrate that even in a mono-domain region, the shallow  $E_u$  mode permits fluctuations in the non-Ising polar components. This is shown in Figure 4(c) where rather than the displacements being clustered at the canonical Ising value, there is a spread in displacement magnitudes in both the Néel and the Bloch directions. Thus, our theoretical calculations demonstrate that polar disorder is intrinsic to  $\text{LiNbO}_3$  and is not just confined to the domain wall proximity.

#### V. PROBABILITY DISTRIBUTION OF POLAR DISPLACEMENTS

The standard accepted method for quantifying disorder is entropy. This can be succinctly expressed through the famous Gibbs-Boltzmann's formulation<sup>31</sup>:

$$S = - \sum_N k_b \rho \log(\rho) \quad (1)$$

where  $S$  is entropy,  $N$  is the number of states,  $k_b$  is the Boltzmann's constant, and  $\rho$  is the probability of a state. Thus a single-state system has zero entropy, while entropy increases with increasing disorder, or increasing number of states. In this work, we measure polar entropy through the quantification of the probabilities of the observed polar displacements ( $\rho$ ), where each possible displacement configuration is a single state. It can thus be deduced also that a monodomain system with a constant value of polar displacement has zero polar entropy.

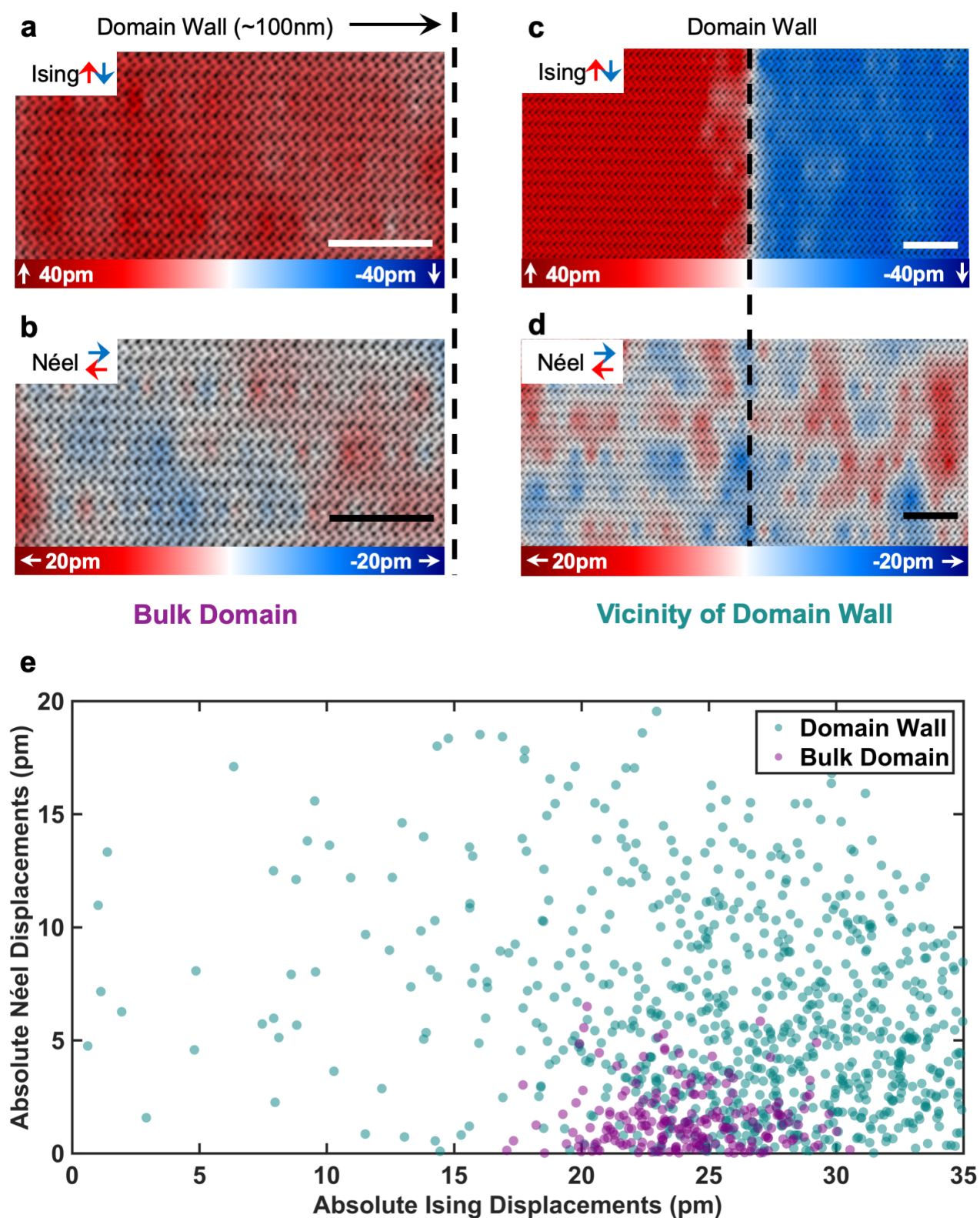


FIG. 3. Comparison of polar displacements at the bulk domain versus the domain wall. (a) - (b) Ising and Néel Nb-O displacements in a region of the bulk domain,  $\approx 100$  nm away from the domain wall. Scale bar is 2 nm. (c) - (d) Ising and Néel Nb-O displacements at the domain wall. Scale bar is 2 nm. (e) Comparison of the absolute magnitudes of the Ising and Néel Nb-O displacements in the two regions imaged in Figure 3(a)-(d) demonstrating the increased variability in displacement magnitudes at the domain wall compared to the bulk domain.

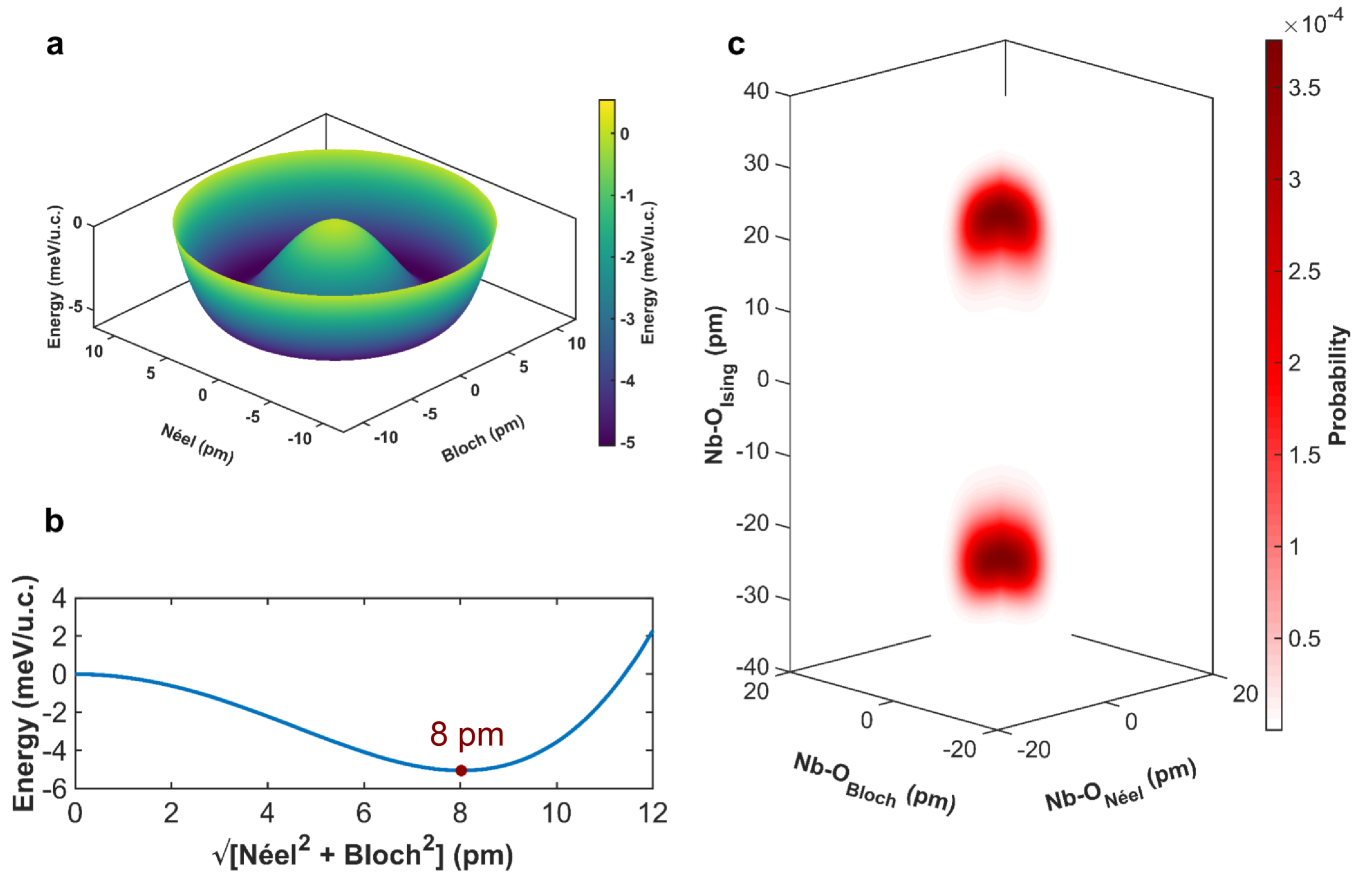


FIG. 4. First Principles Calculations of displacement configurations. (a) Goldstone sombrero potential of the relative energy of  $\text{LiNbO}_3$  with polar Néel and Bloch displacements associated with the  $E_u$  unstable mode. (b) Energy change as a function of the combined Néel and Bloch displacement magnitude, with energy minima at 8pm. (c) Probability of displacements as a function of the Ising, Néel and Bloch displacements from mean field effective Hamiltonian.

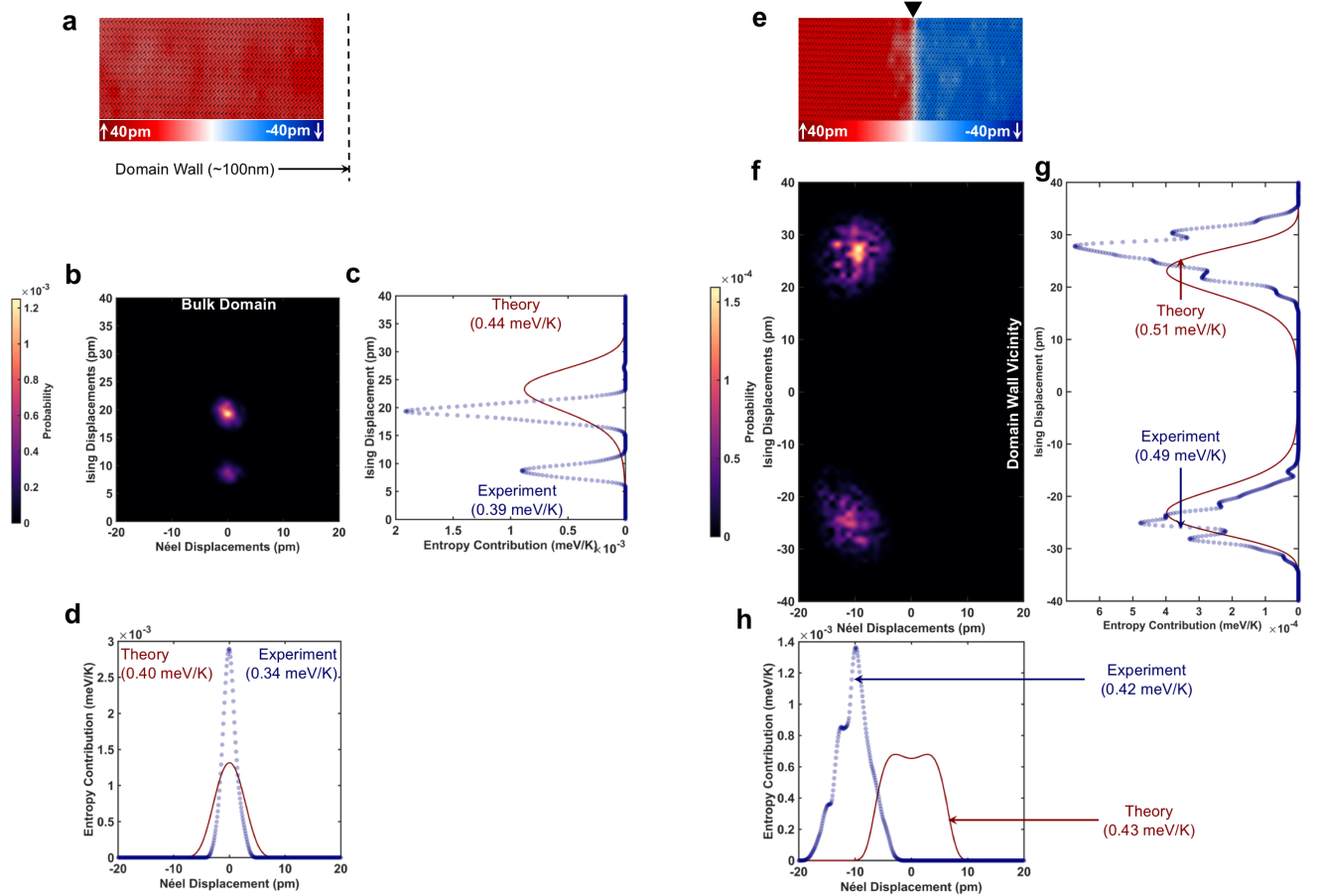


FIG. 5. Measured deconvolved probability and polar entropy in the bulk domain and domain wall proximity in  $\text{LiNbO}_3$ . (a) Representative STEM image of a bulk domain region approximately 100nm to the left of the domain wall from where the probability distribution and entropy was measured with the Ising displacements overlaid demonstrating a monodomain region. Scale bar is 2nm. (b) Richardson-Lucy deconvolved probability distribution of Ising and Néel displacement magnitudes in the bulk domain. (c) - (d) Theoretically calculated (brown) and experimentally measured (blue) entropy contribution as a function of Ising and Néel displacement orientations in the bulk domain, with the summed contribution in inset. (e) Representative STEM image of a region in the proximity of the domain wall with Ising displacements overlaid, with the black triangle marker at the top showing the domain wall location. Scale bar is 2nm. (f) Richardson-Lucy deconvolved probability distribution of Ising and Néel displacement magnitudes in the proximity of the domain wall. (g) - (h) Theoretically calculated (brown) and experimentally measured (blue) entropy contribution as a function of Ising and Néel displacement orientations in the proximity of the domain wall, with the summed contribution in inset. The entropy deconvolution and calculation process is detailed in section B of the appendix.

Experimental quantification of the probabilities ( $\rho$ ) of polar displacements along the Ising and Néel displacement orientations in the bulk domain (representative image shown in Figure 5(a)) is shown in Figure 5(b). The measured displacements do not correspond to one single Ising value and are associated with a spread in Ising and Néel magnitudes with the most probable displacement configuration being 20 pm of Ising displacements and below 5pm of Néel displacements. The Ising displacements demonstrate a bimodal behavior originating from the fluctuations in the  $\langle 0001 \rangle$  intensities that were observed experimentally in the bulk domain. The origin of these fluctuations may be a consequence of local disorder, non-stoichiometry, or vacancy agglomeration in local regions. Further research is required to explain the origin of this Ising bimodal behavior within the bulk domain. Additionally, fluctuations in the electron beam may

overestimate the disorder present in the system.

To measure the effect of the electron beam on the measured entropy, a series of Gaussian probability distributions were deconvolved from the experimentally measured displacements, and the resulting probability distributions that resulted in the lowest entropy value was chosen. Considering the deconvolution of the Gaussian probability distributions, we have calculated a standard deviation ( $\sigma$ ) of 8.7 pm at the bulk domain and 11.7 pm at the domain wall for the microscope instability (detailed in section B). It should be noted that this  $\sigma$  is similar in magnitude to error distributions reported in previous STEM measurements of oxide displacements<sup>32</sup>. The deconvolution procedure thus removes any global fluctuations in the data – which arise notably from microscope instabilities. However, surface damage is expected to create random displacements with no



long-range order as is observed in the experimental analysis. In this experiment the sample damage was minimized by choosing a low final milling energy of 500V (see section A).

The resulting probability distribution after the deconvolution process is used to calculate the polar entropy contribution as a function of the possible Ising and Néel states. Figure 5(c) demonstrates the theoretical and experimental contributions to entropy as a function of Ising displacement configurations, with the total Ising entropy being the sum of the contributions of the individual Ising displacements. Both first principles calculations and experiments demonstrate that a non-zero polar entropy originating from a spread in displacement configurations to be present even in the bulk domain. This picture is repeated even when measuring the entropy arising as a consequence of a spread of Néel displacement probabilities, as shown in Figure 5(d). The integrated entropy associated with the Néel component is measured as 0.31meV/K from experiment, while theory predicts an intrinsic value of 0.4meV/k. The integrated Ising entropy (calculated by integrating the curves in panel Figure 5(c)) are 0.4meV/K (experiment) and 0.44 meV/K (theory). Thus both the measured and theoretically predicted Ising and Néel contributions to the polar entropy are within 10% of each other - indicating the intrinsic nature of these fluctuations.

This picture changes in the proximity of the domain wall (defined here as  $\approx \pm 10\text{nm}$  across the wall - with the STEM image of the representative section shown in Figure 5(e)), whose probability distribution is plotted in Figure 5(f). As expected, we observe a bimodal distribution of the probable polar states in the proximity of the wall owing to two domains being imaged rather than one, with a significantly more diffuse probability distribution as compared to the probabilities measured in Figure 5(b). Both the integrated experimental and the theoretically predicted entropy contributions shown in Figure 5(g) and Figure 5(h) increase in the proximity of the domain wall when compared to the bulk domain. The experimentally measured polar entropy in the proximity of the wall is approximately 28% higher than the bulk domain entropy far away from the wall. In fact, since electron microscopy measurements project a three dimensional object into a 2 dimensions, our measurements underestimate the entropy due to the absence of Bloch displacements in the calculations. This can be understood by the fact, that entropy necessarily refers to random displacements - thus even along the Ising and Néel directions we are measuring a column averaged displacement - not the disorder of individual unit cells. This explains to a certain extent why the experimental entropy measurements are lower than their theoretically predicted values.

## VI. CONCLUSIONS

Our results presented here are the first known experimental quantification of configurational entropy of polar displacements from atomic resolution position metrology. Theoretically predicted and experimentally measured entropy reveals a classical single crystal Ising ferroelectric,

hiding considerable local intrinsic disorder that is present even in the bulk domain. This is despite  $\text{LiNbO}_3$  having only a single symmetry allowed net polarization direction, large coercive fields for domain reversal, and a high Curie temperature indicating its stability at room temperature<sup>27,33-35</sup>. We show that this disorder is intrinsic to ferroelectrics and can exist even in the absence of any extrinsic factors. While previous theoretical studies have demonstrated the effect of entropy in controlling polar behavior halide perovskites, here we demonstrate experimentally that entropy is considerably more prevalent.<sup>36</sup> Polar disorder is a highly sought after component for functional systems like piezoelectrics and electrocalorics, and our study reveals it to be present even in systems thought to be more uniform like  $\text{LiNbO}_3$ <sup>37-40</sup>. The electron microscopy based metrology techniques developed here thus allow for similar studies to be performed in other systems, even beyond ferroelectrics - allowing the electron microscope to be used not only as an imaging system, but also for atomic resolution thermodynamic quantification.

## AUTHOR CONTRIBUTIONS

D.M., V.G. and N.A. designed the project. D.M. prepared the electron microscopy samples, and acquired the transmission electron microscopy data, assisted by K.W. D.M. developed the MATLAB subroutines for analysis. D.M., assisted by L.M., and advised by N.A. and V.G. analyzed the electron microscopy data. S.P., assisted by E.B. performed the first principles calculations. D.M., advised by N.A. and V.G. wrote the manuscript. All authors discussed the results and commented on the manuscript.

## ACKNOWLEDGMENTS

D.M., L.M., V.G. and N.A. would like to acknowledge support from the Penn State Center for Nanoscale Sciences, an NSF MRSEC, funded under the grant number DMR-1420620. S. P. and E.B. acknowledge the supported provided by the University of Liège and the EU in the context of the FP7-PEOPLE-COFUND-BeIPD project, the ARC project AIMED, and the DARPA Grant No. HRO011727183-D18AP00010 (TEE Program) and the Céci facilities funded by F.R.S-FNRS (Grant No. 2.5020.1) and Tier-1 supercomputer of the Fédération Wallonie-Bruxelles funded by the Walloon Region (Grant No. 1117545). D.M., V.G. and N.A. would like to acknowledge the Penn State Materials Characterization Laboratory for use of their sample preparation and electron microscopy facilities. D.M. would like to acknowledge Dr. Haiying Wang of Penn State Materials Characterization Laboratory for help with sample preparation.

## Appendix A: Electron Microscopy of $\text{LiNbO}_3$

For this study, we used commercially available periodically poled single crystal congruent  $\text{LiNbO}_3$  crystals with  $6.7\mu\text{m}$

domain repetition from Deltronic Industries. The electron transparent samples were prepared by focused ion beam (FIB) using a FEI Helios G2 system with a 30keV gallium ion beam used for sample lift-out with the domain walls lying edge on. Final polishing was performed with 0.5kV ion beams till the sample became electron transparent at an accelerating of 2kV to ensure that the sample was thin enough for imaging oxygen atoms<sup>41</sup>. FIB was chosen for it's advantage in site specific sample preparation. The extent of amorphous surface damage is proportional to the ion accelerating voltage - at low energies such as 2kV, the amorphous layer thicknesses are approximately 0.5–2nm thick<sup>42,43</sup>. A recent work has demonstrated that low voltage ion milling at 0.4kV completely eliminated amorphous surface layers<sup>44</sup>. In fact FIB has been recently used for preparing battery electrolyte TEM samples too, with no apparent damage to the sample<sup>45</sup>. The prepared samples were found to have a sample thickness ranging between 20-25nm, as estimated with EELS inelastic mean free path measurements (Figure 7)<sup>24</sup>.

Following the preparation of electron transparent samples, we first imaged the LiNbO<sub>3</sub> foil with conventional TEM (CTEM) mode at a slight defocus to locate and identify the domain walls from their diffraction contrast. Following the identification of the domain walls, we subsequently used STEM imaging in a spherical aberration corrected FEI Titan<sup>3</sup> transmission electron microscope, corrected for upto third order spherical aberrations. Annular dark Field Scanning TEM (ADF-STEM) imaging was performed using Fischione detectors at a camera length of 145mm with an inner collection semi-angle of 32mrad, and an outer collection semi-angle of 188 mrad. Bright Field Scanning TEM (BF-STEM) images were simultaneously collected with Gatan detectors with an outer collection semi-angle of 15mrad. Simultaneous BF-STEM and ADF-STEM imaging was performed with fast scan directions oriented at  $-5^\circ$  and  $85^\circ$  with respect to the  $\langle 11\bar{2}0 \rangle$  crystallographic axis. The two image sets were combined and subsequently corrected post acquisition for scan drift using a previously developed procedure<sup>46</sup>. After acquiring the atomic resolution BF-STEM images, we used MATLAB scripts to refine the positions for sub-pixel precision displacement metrology. To perform the refinement, we started by locating the highest intensity spots as a first pass to estimate atom positions in ADF-STEM and inverted contrast BF-STEM images. We performed subsequent refinement by fitting a multi-peak two-dimensional Gaussian to the observed atom intensity distribution to get the atom positions with a precision approaching  $\approx 2\text{pm}$ <sup>32</sup>.

## Appendix B: Quantification of Polar Entropy

Entropy measurements are performed using STEM data acquired at both the domain wall and the bulk domain. Since the average pixel size for the experimental setup is approximately 10pm, and the approximate image size is approximately  $2000 \times 2000$  pixels, a representative image can visualize a  $400\text{nm}^2$  area. Thus images captured at the domain wall with the domain wall centered in the image field

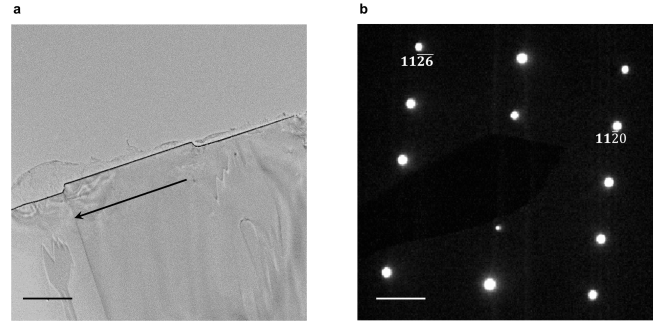


FIG. 6. Low magnification TEM image and electron diffraction pattern. (a) Low magnification CTEM with the domain wall (marked by the arrow) visible due to diffraction contrast at the wall. (b) Diffraction pattern from the image in Figure 6(a) confirming the  $[1\bar{1}00]$  zone axis.

of view, still have approximately 10nm of the domain on either side. Entropy calculations are performed on one full image, and thus domain wall entropy measurements also include contributions from approximately 10nm of the domain on either side of the boundary. On average, the BF-STEM images from our experimental conditions correspond to approximately 800 unit cells. The polar displacements at each of the individual locations were subsequently sorted into 0.1pm bins, from -50pm (minimum) to 50pm (maximum) of displacement magnitude - both for Ising and Néel displacements with a total of  $1001 \times 1001$  possible displacement configurations. Thus, if a certain unit cell corresponds to an Ising displacement of 25.386pm, and a Néel displacement of -12.456pm, it will be assigned to the bin corresponding to the displacements of 25.3 to 25.4 Ising displacements, and -12.5 to -12.4pm of Néel displacements with one unit cell corresponding to one displacement observation. Following assignment of all the observed displacements for one full image into their respective bins, the total number of observations for each bin is divided by the total observations made for the entire image. This is the probability ( $\rho$ ) of observing a displacement corresponding to that bin position.

To quantify the effect of displacement bin size in estimating the entropy, we redid the calculations on one of the datasets – Ising entropy calculations at the domain wall with varying bin sizes from 0.1pm to 1pm as shown in Figure 8. Choosing a 1pm bin size, rather than a 0.1pm bin size results in a reduction of the entropy from 0.567 meV/K to 0.539 meV/K, which is  $\approx$  a 5% reduction in the measured entropy. Thus, we can see that the entropy we measure is almost independent of the bin size. This can be explained by the fact that while the entropy contribution term ( $k_b \rho \log(\rho)$ ) in Equation 1 from a single displacement bin increases with increasing the bin size due to an increase of the displacement probability  $\rho$  – however this also leads to a reduction in the total number of displacement bins ( $N$ ), and thus the entropy which is integrated over all the possible displacement values remains fairly constant.

A shortcoming of this technique is however rooted in the fact that the measured entropy is a function of the total

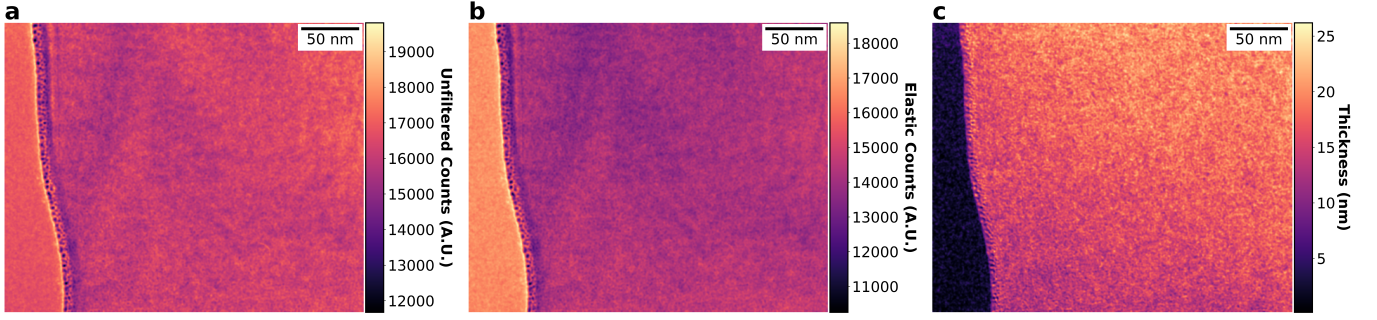


FIG. 7. Quantification of sample thickness through EELS. (a) Low mag unfiltered (zero-loss and core-loss) EFTEM image. (b) Simultaneously acquired elastic scattering (zero-loss) EFTEM image. (c) Quantified thickness from the log of the ratio of the total inelastic and elastic (Figure 7(a)) and elastic (Figure 7(b)) scattering contributions, demonstrating an average thickness of approximately 20-25 nm throughout the sample<sup>24</sup>.

observed vibrational probability – which is a combination of the *intrinsic* disorder of the system itself, instabilities in the electron microscope, and induced entropy originating from the interaction between the crystal and the electron beam. While it is the intrinsic material entropy that we ideally want to measure, because of the two latter effects our measured entropy overestimates the entropy in the system. Since these measurements were performed using a single crystal of LiNbO<sub>3</sub> where there is a remnant intrinsic entropy even in the bulk domain, there is no reference lattice to measure the microscope instabilities.

In fact even a reference lattice measurement may underestimate entropy — for example, SrTiO<sub>3</sub>, an ubiquitous oxide substrate is an incipient ferroelectric, with thin freestanding SrTiO<sub>3</sub> being a ferroelectric<sup>47</sup>. Polar fluctuations may not be limited to LiNbO<sub>3</sub> only, and it is highly conceivable that an entropy measurement of the substrate will also measure the intrinsic polar fluctuations of the substrate and thus overestimate microscope vibrations.

To estimate the contribution from measurement we assume that the instabilities can be expressed as a two-dimensional Gaussian distribution with a  $\sigma_x$  and a  $\sigma_y$ . The same assumption was also made for electron beam induced atom vibrations - and this is justified since the Debye-Waller parameters for both Niobium and Oxygen ( $u_{\text{Nb}} = 0.3924$  and  $u_{\text{O}} = 0.5$ <sup>48</sup>) can be approximated as scalars rather than tensors<sup>48</sup>. Since the convolution of a Gaussian kernel with another co-located Gaussian kernel is also a Gaussian, thus the total non-intrinsic microscope instability contribution ( $\rho_{x,y}$ ) can be reasonably approximated as a two-dimensional Gaussian function where  $x$  and  $y$  are the Cartesian displacement directions.

Thus, the Gaussian function can be written as:

$$\rho_{x,y} = \frac{1}{\sqrt{2\pi}\sigma} e^{-\frac{1}{2}\left(\left(\frac{x-\mu_x}{\sigma_x}\right)^2 + \left(\frac{y-\mu_y}{\sigma_y}\right)^2\right)} \delta x \delta y \quad (\text{B1})$$

This is a probability distribution, since:

$$\int_{-\infty}^{\infty} \int_{-\infty}^{\infty} \rho_{x,y} = \int_{-\infty}^{\infty} \int_{-\infty}^{\infty} \frac{1}{\sqrt{2\pi}\sigma} e^{-\frac{1}{2}\left(\left(\frac{x}{\sigma_x}\right)^2 + \left(\frac{y}{\sigma_y}\right)^2\right)} \delta x \delta y \quad (\text{B2})$$

$$= 1 \quad (\text{B3})$$

Since this is the microscope instability probability, the Gaussian is centered at  $(\mu_x, \mu_y) = 0$ , then Equation B1 can be expressed as:

$$\rho_{x,y} = \frac{1}{\sqrt{2\pi}\sigma} e^{-\frac{1}{2}\left(\left(\frac{x}{\sigma_x}\right)^2 + \left(\frac{y}{\sigma_y}\right)^2\right)} \delta x \delta y \quad (\text{B4})$$

Using the Boltzmann definition of entropy, and inputting Equation B4 in Equation 1

$$\Delta S_e = k_B \left[ \log(\sqrt{2\pi}\sigma_x + \sigma_y) + \frac{1}{2} \right] \quad (\text{B5})$$

where  $\Delta S_e$  refers to the microscope contribution to measured entropy.

Thus, as Equation B5 demonstrates, the total entropy increases monotonically with  $\sigma_x$  and  $\sigma_y$ . To obtain the intrinsic probability, a deconvolution of the measured probability distribution function with a Gaussian PDF is thus required. It can be easily deduced that the microscope contribution to the entropy is mathematically analogous to a blurring function commonly encountered in optics. Thus, the experimentally measured probability is the material probability convolved by a point spread function (PSF) of the instrumental vibrations, with the PSF assumed to be Gaussian in this case. To deconvolve the underlying entropy, we can thus use the Richardson-Lucy deconvolution to iteratively obtain the unblurred PDF<sup>49,50</sup>. Mathematically, thus if  $\rho$  is the microscope instability probability distribution, and  $\tau$  is the intrinsic fluctuation in polar displacements, it is the following entropy we are after.

$$\Delta S_i = \int k_B \tau \log \tau \quad (\text{B6})$$

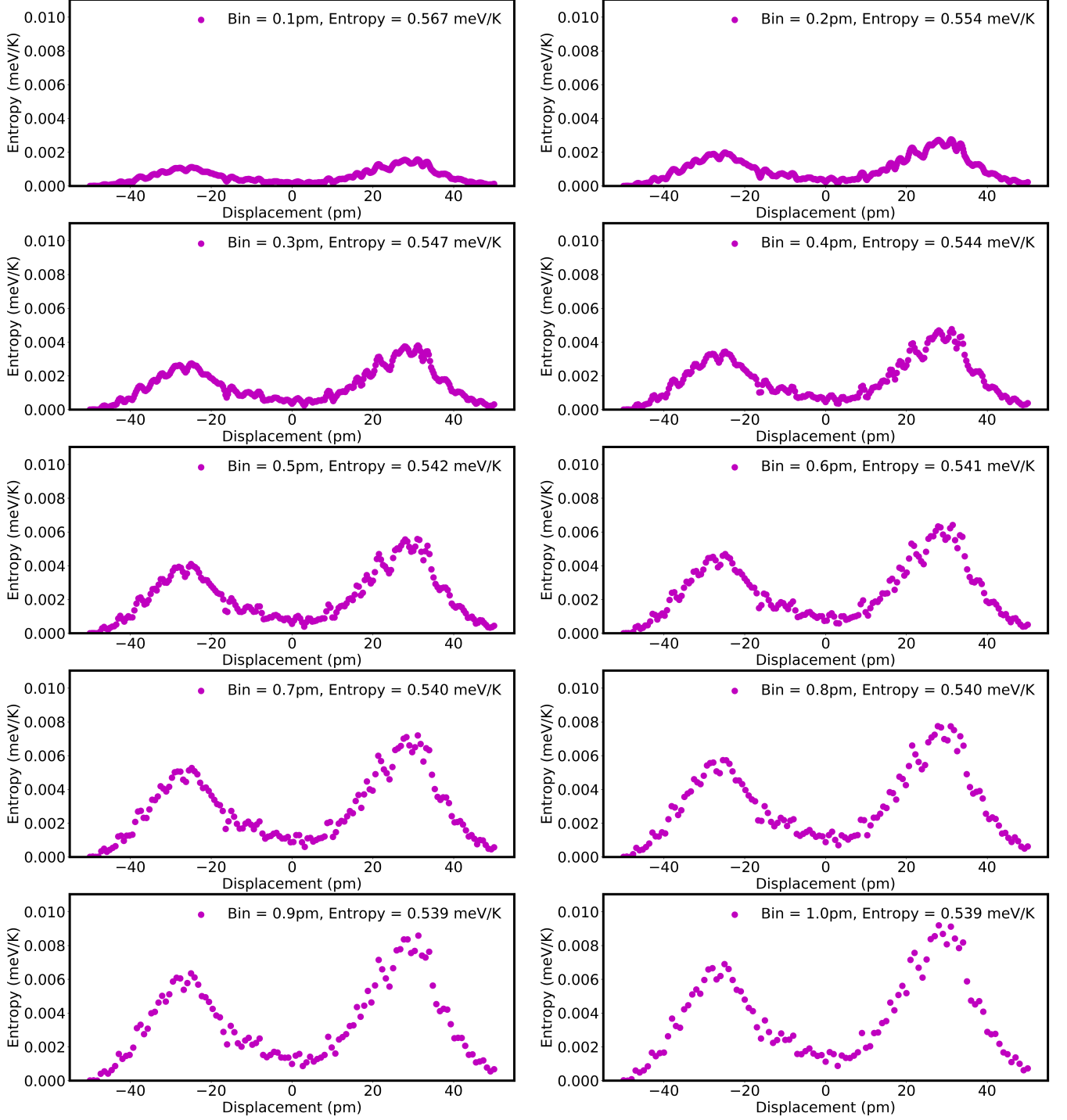


FIG. 8. Measured polar entropy for Ising displacements at the domain wall as a function of the displacement bin size, ranging from 0.1pm bin size to 1pm bin size.

Since, the measured probability distribution  $\phi$  is a convolution, it can be written as:

$$\phi = \theta \circ \rho \quad (\text{B7})$$

$$= \mathcal{F}(\mathcal{F}^{-1}(\tau) \times \mathcal{F}^{-1}(\rho)) \quad (\text{B8})$$

Thus for a certain value of  $\sigma_x$  and  $\sigma_y$ , the deconvolved

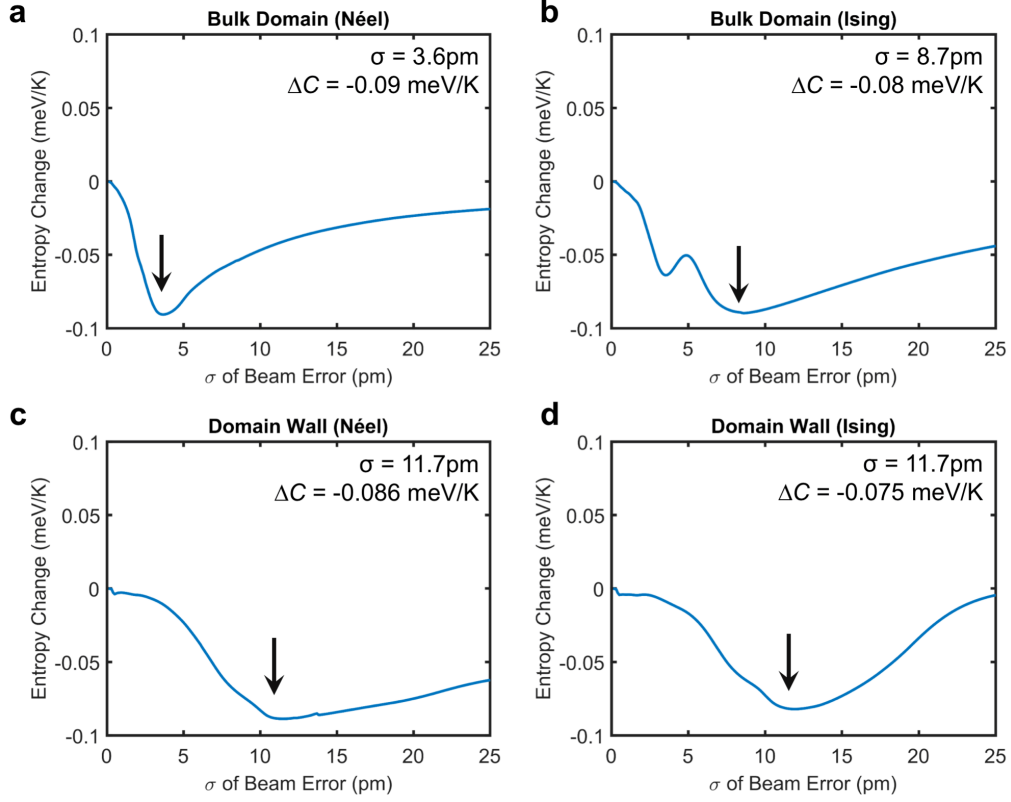


FIG. 9. Plotting the decrease in entropy as a function of the beam effects. (a) Change in measured entropy as a function of the measured  $\sigma$  of the Gaussian of the beam probability function for Néel displacements inside the bulk domain ( $\approx 100\text{nm}$  away from the domain wall.). The minima is at  $3.6\text{pm}$ . (b) Change in measured entropy as a function of the measured  $\sigma$  of the Gaussian of the beam probability function for Ising displacements inside the bulk domain ( $\approx 100\text{nm}$  away from the domain wall.). There are two minima — at  $3.6\text{pm}$  and  $8.7\text{pm}$ . (c) Change in measured entropy as a function of the measured  $\sigma$  of the Gaussian of the beam probability function for Néel displacements in the proximity of the domain wall. The minima is at  $11.7\text{pm}$ . (d) Change in measured entropy as a function of the measured  $\sigma$  of the Gaussian of the beam probability function for Ising displacements in the proximity of the domain wall. The minima is at  $11.7\text{pm}$ .

probability as a function of  $\sigma_x$  and  $\sigma_y$  can be expressed as

$$\tau_{\sigma_x, \sigma_y} = \mathcal{F} \left( \frac{\mathcal{F}^{-1}(\phi) \times \left( \mathcal{F}^{-1}(\rho_{\sigma_x, \sigma_y}) \right)^*}{|\mathcal{F}^{-1}(\rho_{\sigma_x, \sigma_y})|^2} \right) \quad (\text{B9})$$

where  $\mathcal{C}^*$  is the complex conjugate of a function  $\mathcal{C}$ .

Thus, the decrease in entropy  $\Delta C$  as a result of the deconvolution :

$$\Delta C_{\sigma_x, \sigma_y} = -k_B \left( \int \phi \log \phi - \int \tau_{\sigma_x, \sigma_y} \log \tau_{\sigma_x, \sigma_y} \right) \quad (\text{B10})$$

Since we do not possess a reference lattice from which a point spread function could be deduced, we measured  $\Delta C_{\sigma_x, \sigma_y}$  for both Ising and Néel displacements in the bulk domain and at the domain wall. For Néel displacements in the bulk domain, the  $\Delta C_{\sigma_x, \sigma_y}$  reaches a minima with a  $\sigma_x = 3.6\text{pm}$  as demonstrated in Figure 9(a). Qualitatively, this means that the PDF corresponding to this particular displacement can be most closely be approximated a Gaussian of  $\sigma_x = 3.6\text{pm}$ . Compared to the Néel displacements, when

we plot  $\Delta C_{\sigma_x, \sigma_y}$  for Ising displacements in the bulk domain in Figure 9(b), we encounter two minima - one identical to the minima in Figure 9(a) at  $3.6\text{pm}$ , and the second minima at  $8.7\text{pm}$ . The origin of this behavior could be understood by looking at the probability distribution of Ising displacements in the bulk domain (Figure 5(b) & Figure 5(c)) which is bimodal. For the most conservative possible estimate, thus all domain probabilities were calculated after deconvolving the measured probability distribution with a Gaussian of  $\sigma_x = 3.6\text{pm}$  and  $\sigma_y = 8.7\text{pm}$ .

Extending the deconvolution to the proximity of the domain wall, we observe that the maximum decrease in entropy occurs for both Néel and Ising displacements when the measured probability distribution function is deconvolved with a Gaussian with  $\sigma = 11.7\text{pm}$ . It is interesting to note that the  $\sigma_x$  and  $\sigma_y$  is larger in the proximity of the domain wall, than in the bulk domain. However, since the experimental data for both regions was acquired back to back in the same experimental session - it is highly unlikely that the microscope is quantifiably less stable at the domain wall than at domain. Rather, any Gaussian features in the proba-

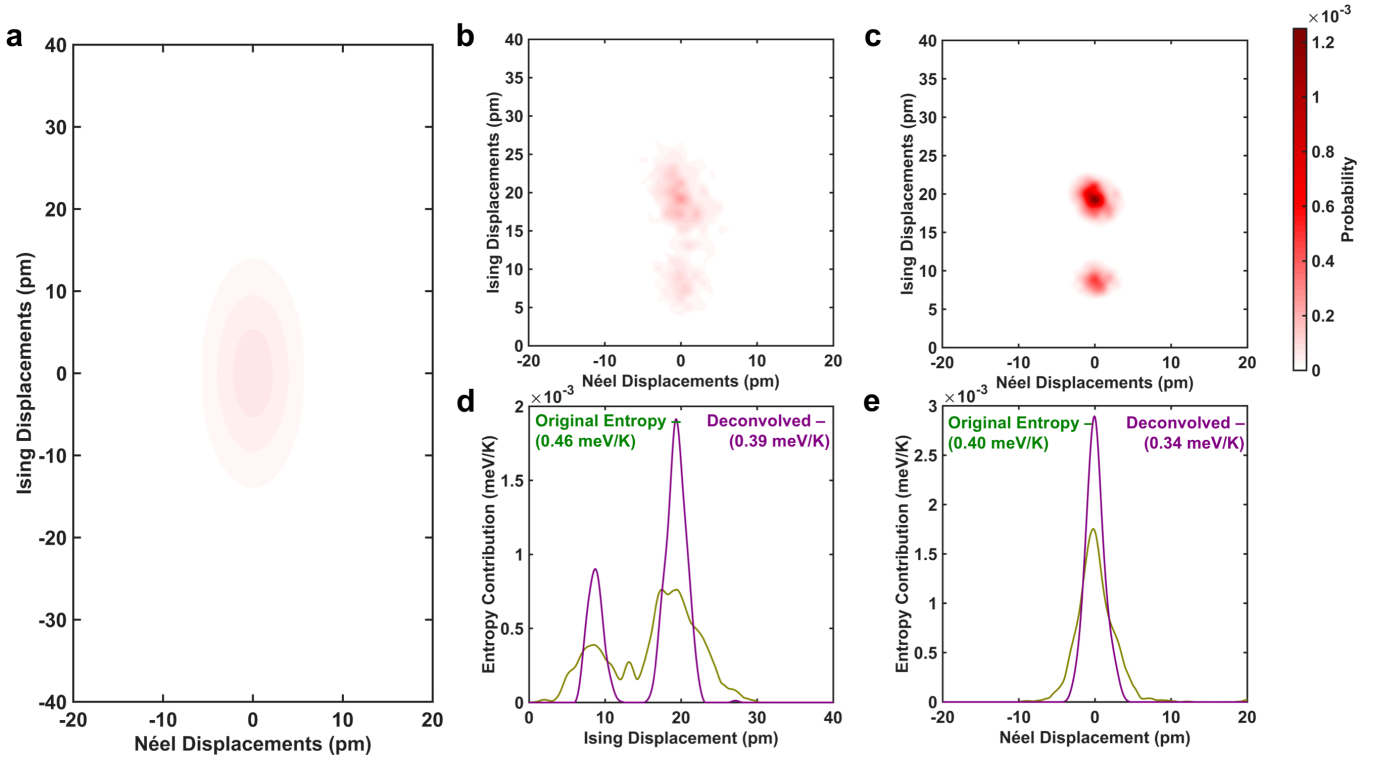


FIG. 10. Deconvoluting the microscope effects in the bulk domain. (a) Gaussian estimation of the microscope instabilities with  $\sigma_{\text{Neel}} = 3.6\text{pm}$  and  $\sigma_{\text{Ising}} = 8.7\text{pm}$ . (b) Experimentally calculated probability distribution of polar displacements in the bulk domain. (c) Richardson-Lucy deconvolved probability distribution of polar displacements in the bulk domain. (d) Comparison of original and deconvolved entropy measurements as a function of Ising displacements, demonstrating an  $\approx 13\%$  reduction in entropy. (e) Comparison of original and deconvolved entropy measurements as a function of Néel displacements, demonstrating an  $\approx 23\%$  reduction in entropy.

bility distribution function are in fact being assigned to the point spread function, and thus this technique of measuring entropy is actually slightly conservative – the deconvolved entropy is in reality *underestimating* the intrinsic material entropy.

Visually, we can understand the effect of the deconvolution by observing the  $\sigma_x = 3.6\text{pm}$  and  $\sigma_y = 8.7\text{pm}$  Gaussian distribution in Figure 10(a), the original measured probability distribution in Figure 10(b) and the deconvolved probability in Figure 10(c) in the bulk domain. The deconvolved probability is significantly sharper and less spread out. This is borne out by a reduction of the Ising contribution of the entropy from  $0.46\text{meV/K}$  to  $0.40\text{meV/K}$ , a reduction of  $\approx 13\%$ , as demonstrated in Figure 10(d). The Néel contribution to the entropy, plotted in Figure 10(e) also declines by  $\approx 23\%$  from  $0.40\text{meV/K}$  to  $0.31\text{meV/K}$ .

Similarly, plotting the effects of the  $\sigma_x, \sigma_y = 11.7\text{pm}$  Gaussian point spread function in the proximity of the domain wall, we find a marked sharpening of the deconvolved probability distribution function in Figure 11(c) when compared to the experimentally measured probability distribution in Figure 11(b). This sharpening leads to a reduction of the Ising contribution to the entropy, as plotted in Figure 11(d) by  $14\%$  from  $0.57\text{meV/K}$  to  $0.49\text{meV/K}$ . The Néel contribution to the entropy, plotted in Figure 11(e), declines by  $16\%$  as a result of the deconvolution from  $0.50\text{meV/K}$  to  $0.42$

$\text{meV/K}$ . Thus, while the deconvolution decreases the total measured entropy across the board, even using the most aggressive Gaussian kernel does not result in zero entropy, showing that this polar entropy is intrinsic to the material itself.

Thus, we observe around  $\approx 25\%$  reduction in the measured entropy due to the deconvolution. The entropy of displacements ( $S$ ) were subsequently calculated from the deconvolved probability distributions as per Equation 1.

### Appendix C: First principles calculations

First principles calculations were done using the density functional theory approximation as implemented in the ABINIT software package (v.8.4.3)<sup>51–54</sup>. We chose the libxc implementation of PBEsol GGA functional to describe the exchange-correlation energy contribution, and the valence electrons were treated through norm-conserving pseudopotentials obtained through the PseudoDojo project<sup>55–59</sup>. The planewave kinetic cut-off energy was taken to be equal to  $50\text{Ha}$  and the Brillouin zone was sampled using a  $6 \times 6 \times 6$  Monkhorst-Pack mesh of special  $k$  points<sup>60</sup>. To determine the structure of the paraelectric  $R\bar{3}c$  phase structure of  $\text{LiNbO}_3$ , we considered a primitive 10 atom unit cell and performed a relaxation of atomic positions followed by an energy opti-

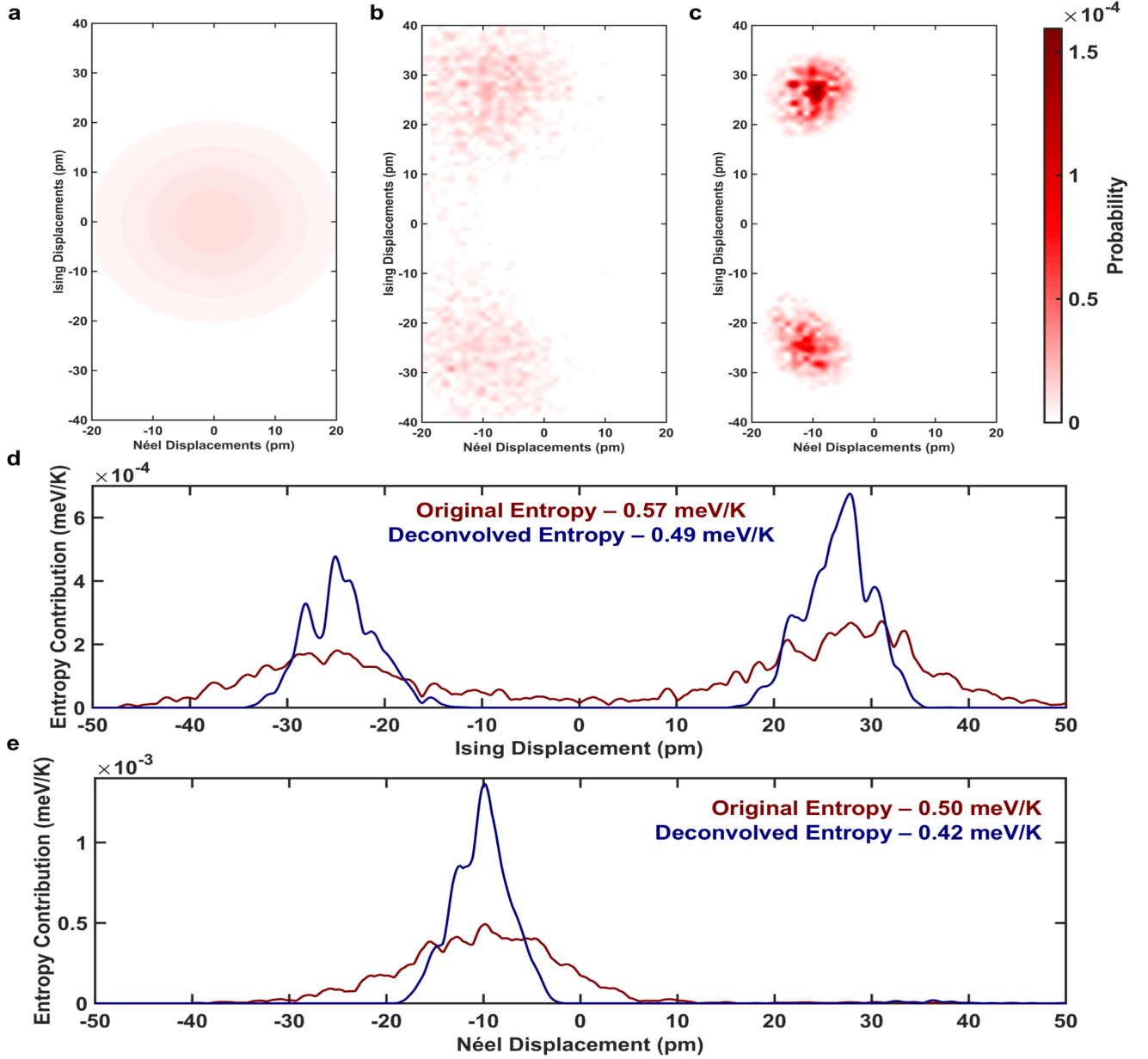


FIG. 11. Deconvoluting the microscope effects in the proximity of the domain wall. (a) Gaussian estimation of the microscope instabilities with  $\sigma_{\text{Ising}} = \sigma_{\text{Néel}} = 11.7\text{pm}$ . (b) Experimentally calculated probability distribution of polar displacements in the proximity of the domain wall (c) Richardson-Lucy deconvolved probability distribution of polar displacements in the proximity of the domain wall. (d) Comparison of original and deconvolved entropy measurements as a function of Ising displacements, demonstrating an  $\approx 14\%$  reduction in entropy. (e) Comparison of original and deconvolved entropy measurements as a function of Néel displacements, demonstrating an  $\approx 16\%$  reduction in entropy.

mization with respect to changes both in lattice vectors and the reduced atomic coordinates under an imposed constraint of the fixed  $R\bar{3}c$  space-group symmetry, with the primitive unit cell dimensions given in Table I. The high-accuracy structural relaxation was performed until the calculated force magnitudes were less than  $10^{-8}\text{eV}$  per  $\text{\AA}$ , and the absolute values of stress tensor components do not exceed  $10^{-7}\text{GPa}$ . We performed density functional perturbation

theory calculations (DFPT) so as to identify the unstable phonon modes (Table II). To construct the minimal effective Hamiltonian model we have first computed the internal energy landscapes for all identified unstable modes. For this, we have performed DFT calculations of the total energy change upon gradually condensing the unstable modes into the structure. The resulting curves were fitted with the 8<sup>th</sup> order polynomials as given by Equation C1.

Atom Position	
Li1	(0, 0, $1/2$ )
Nb1	(0, 0, 0)
O1	( $-1/3$ , $-1/3 + x$ , $7/12$ )
O2	( $1/3 - x$ , $-x$ , $7/12$ )
O3	( $x$ , $1/3$ , $7/12$ )

TABLE I. Calculated hexagonal co-ordinates of atoms of the primitive unit cell of paraelectric LiNbO<sub>3</sub>. The lattice parameters are  $a = 518\text{pm}$  and  $c = 1364.6\text{pm}$ .

$$E_M = \kappa_M x^2 + \alpha_M x^4 + \gamma_M x^6 + \delta_M x^8 \quad (\text{C1})$$

where  $x$  denotes the amplitude of the mode  $M$ . Similarly, performing calculations of energy changes induced by displacements involving not a single but two phonon modes allows to reconstruct the effective mode interactions that we take here to be of the form

$$E_{int}^{M_1 M_2} = g_{M_1 M_2} x^2 y^2 \quad (\text{C2})$$

where  $x$  and  $y$  denote the amplitudes of the  $M_1$  and  $M_2$  modes. The interaction of local modes with strain is taken into account by fitting the dependences of elastic stresses on the mode amplitudes. Finally, the elastic energy produced by the deformations of the cell shape and volume is taken into account in the harmonic approximation. The elastic constants are computed from density functional perturbation theory. Note that in the case of the  $E_u$  mode, all the energy expansion coefficients are assumed to depend on the displacement direction in the (0001) plane, however the calculations show that such in-plane anisotropy can be safely neglected. In the described model, the short-range and long-range dipolar interactions between different modes are taken into account in the mean-field approximation – these energetic contributions essentially lead to renormalization of the  $\kappa_M$  and  $f_{M_1 M_2}$  coefficients. To determine the most important low-energy atomic displacements patterns we further performed the density functional perturbation theory calculations so as to identify low frequency phonon modes for the obtained ground state.

#### Appendix D: Calculation of polar modes

The calculated polar modes for the paraelectric LiNbO<sub>3</sub> unit cell (Table I) are shown in Table II. As could be observed, there are four polar modes, with the  $A_{2u}$  mode driving ferroelectricity, while it is the degenerate  $E_u$  modes that drive the non-Ising Néel and Bloch displacements. The polar phonon mode displacements are visualized in Figure 12, which plot the individual atom displacements corresponding to the polar modes.

Atom	Polar Phonon Modes			
	$A_{2g}$	$A_{2u}$	$E_u$	$E_u$
Li1	(0.000)	(0.000)	(0.000)	(0.069)
	(0.000)	(0.000)	(-0.069)	(0.000)
Li2	(0.407)	(0.683)	(0.000)	(0.000)
	(0.000)	(0.000)	(-0.069)	(0.000)
Nb1	(0.000)	(0.000)	(-0.384)	(-0.356)
	(0.000)	(0.000)	(0.356)	(-0.384)
Nb2	(0.259)	(0.000)	(0.259)	(0.000)
	(0.000)	(0.000)	(0.384)	(-0.356)
O1	(0.000)	(0.000)	(0.356)	(0.384)
	(0.000)	(0.000)	(0.000)	(0.000)
O2	(0.029)	(0.055)	(0.002)	(0.269)
	(0.017)	(0.032)	(-0.272)	(-0.002)
O3	(-0.297)	(-0.085)	(0.012)	(-0.021)
	(-0.029)	(-0.055)	(-0.002)	(0.269)
O4	(0.017)	(-0.032)	(-0.272)	(0.002)
	(-0.297)	(0.085)	(-0.012)	(-0.021)
O5	(0.000)	(0.000)	(0.000)	(0.274)
	(-0.033)	(-0.064)	(-0.268)	(0.000)
O6	(-0.297)	(-0.085)	(-0.024)	(0.000)
	(0.000)	(0.000)	(0.000)	(0.274)
O7	(-0.033)	(0.064)	(-0.268)	(0.000)
	(-0.297)	(0.085)	(-0.024)	(0.000)
O8	(-0.029)	(-0.055)	(-0.002)	(0.269)
	(0.017)	(0.032)	(-0.272)	(0.002)
O9	(-0.297)	(-0.085)	(0.012)	(0.021)
	(0.029)	(-0.055)	(0.002)	(0.269)
O10	(0.017)	(-0.032)	(-0.272)	(-0.002)
	(-0.297)	(0.085)	(0.012)	(-0.021)

TABLE II. Eigenvectors in Cartesian coordinates of the identified unstable phonon modes of paraelectric LiNbO<sub>3</sub>.

#### Appendix E: Displacements in the Bulk Domain

Two different regions (Figure 13 and Figure 14) are shown as different regions of the bulk domain that were imaged. While all three are mono-domain regions, it is instructive to note that the Ising displacement itself is not entirely constant even 100nm into the domain, with the displacement demonstrating magnitude variations as seen in Figure 13(a). These regions are additionally associated with regions of Néel displacements as can be observed in Figure 13(b). These Néel displacements are ultimately visible in the rotation map (see Figure 13(c)), demonstrating polar non-Ising components arising even in bulk domain regions approximately 100nm away from the domain wall. This variation in polar components is ultimately reflected in increased entropy.

Figure 14 demonstrates a section of the bulk domain, approximately 20nm away from the domain wall. As could be observed in this section, the total Ising displacements are significantly smaller than expected, with a corresponding decrease in Néel displacements, demonstrating regions of decreased polarity embedded in the domain near the domain wall.



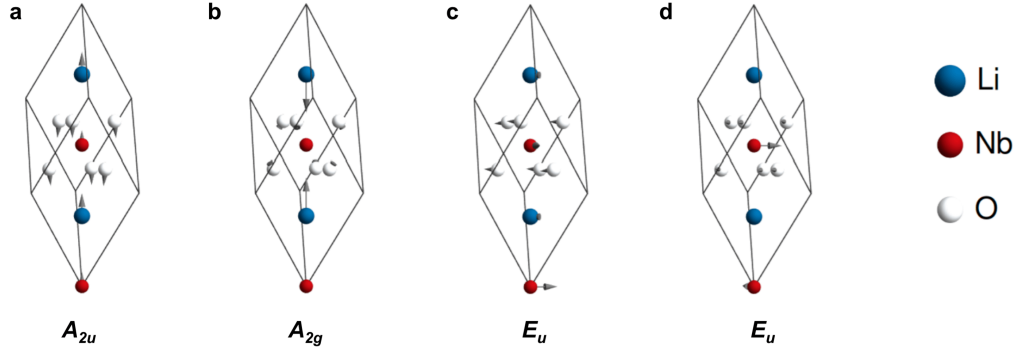


FIG. 12. Eigenvectors of the phonon modes. (a) the  $A_{2u}$  mode. (b) the  $A_{2g}$  mode. (c) and (d) the two eigenvectors corresponding to the degenerate  $E_u$  mode aligned with x and y Cartesian axis respectively.

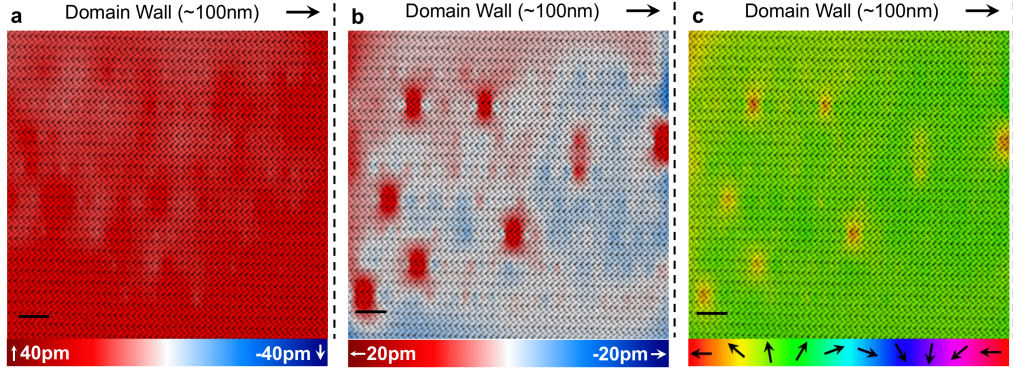


FIG. 13. Bulk domain HR-STEM image with the polarization and rotation map overlaid on top at a location  $\approx 100\text{nm}$  away from wall. (a) Ising displacement mapped out over the bulk domain. (b) Néel displacement map showing regions of no Néel displacements, and nanoregions of high Néel displacements. (c) Rotation colormap. Scale bar in all images is 2nm.

#### Appendix F: Displacements in the the proximity of the Domain Wall

Four other domain wall regions (labeled as regions 2-5) in addition to the region imaged in the main text (Figure 2) were imaged in the electron microscope, as demonstrated in Figure 15, Figure 16, Figure 17 and Figure 18. As could be observed from all the systems the domain wall is consistently associated with significant Néel type non-Ising distortions. One of the regions of the domain wall, Figure 15 also demonstrates Néel distortions in both positive and negative directions, with leftward Néel distortions precipitating primarily at the domain wall. Also, the thickness of the Ising component at the domain wall is not uniform at different regions of the domain wall, with Figure 16 demonstrating significantly wider walls compared to the other regions imaged.

#### Appendix G: Estimation of charge accumulation and electrostatic potential energy

We roughly estimated the charge accumulation from the polar distortions to get an estimate in the energy magnitudes of electrostatic potential energy and the thermodynamic free

energy decrease from the entropy.

Charge calculations were performed by first estimating the Born effective charge tensors theoretically, with the calculated Born effective charges presented in Table III. The calculated polar displacements from a representative bulk domain region (Figure 13) and a representative domain wall region (Figure 2) respectively are vector multiplied with the Born effective charge tensors (Table III) for the niobium and oxygen atoms only, since we cannot image the lithium atoms. The divergence of this polarization is now the charge accumulation, which is presented in Figure 19, with Figure 19(a) showing the charge accumulation in the bulk domain region, and Figure 19(b) demonstrating the charge accumulation in the domain wall proximity.

Thus, for each image, we have a total charge distribution. Assuming that each pixel corresponds to a charge value, then the total number of pixels ( $N$ ) refers to the total possible charge values. The electrostatic potential energy is then calculated using Equation G1, obtained through an integration of Coulomb's law

$$U_E = \frac{1}{2} \sum_{x=1}^N q_x \sum_{y=1}^{N(y \neq x)} \left( \frac{1}{4\pi\epsilon_0\epsilon_{\text{LiNbO}_3}} \times \frac{q_y}{r_{xy}} \right) \quad (\text{G1})$$

where  $q_x$  refers to the charge at a certain pixel, and  $r_{xy}$  refers

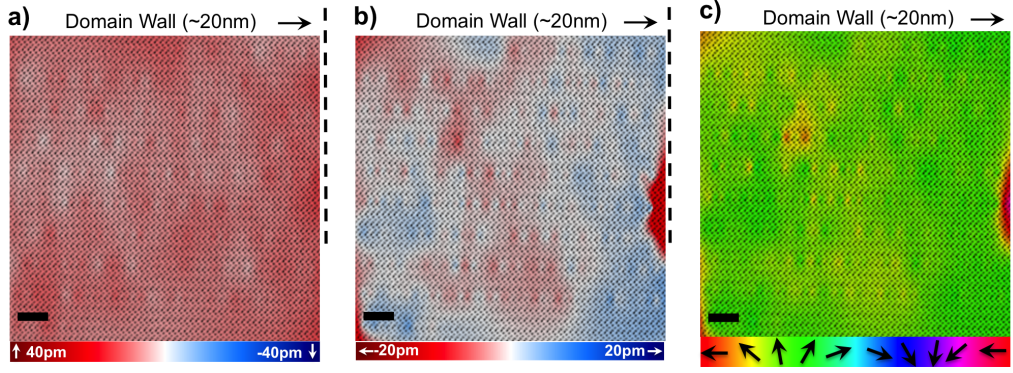


FIG. 14. Bulk domain  $\approx 20\text{nm}$  away from wall. (a) Ising displacement mapped out over the bulk domain, showing significantly lower displacements in comparison to other imaged regions. (b) Néel displacement map showing regions of lower Néel displacements. (c) Rotation color map. Scale bar in all images is  $2\text{nm}$

Atom	Cartesian Direction	Born Effective Charge		
		1	2	3
Li	1	1.150619	$-1.860690 \times 10^{-16}$	$5.756686 \times 10^{-16}$
	2	$-1.364568 \times 10^{-16}$	1.150619	$4.525044 \times 10^{-16}$
	3	$1.097943 \times 10^{-16}$	$1.898622 \times 10^{-13}$	-1.103018
Nb	1	8.330707	-2.061953	$2.317528 \times 10^{-16}$
	2	2.061953	8.330707	$3.418674 \times 10^{-16}$
	3	$-8.225340 \times 10^{-1}$	$3.464213 \times 10^{-12}$	9.199131
O1	1	-3.848460	-1.191682	-2.153211
	2	-1.191682	-2.472424	-1.243157
	3	-2.048031	-1.182431	-3.434050
O2	1	-1.784406	$-3.133223 \times 10^{-17}$	$2.586606 \times 10^{-16}$
	2	$1.249054 \times 10^{-17}$	-4.536477	2.486314
	3	$1.357373 \times 10^{-16}$	2.364863	-3.434050
O3	1	-3.848460	1.191682	2.153211
	2	1.191682	-2.472424	-1.243157
	3	2.048031	-1.182431	-3.434050

TABLE III. Calculated Born effective charges in  $\text{LiNbO}_3$

to the distance between the  $x^{\text{th}}$  and the  $y^{\text{th}}$  pixel. The term  $1/2$  prevents double counting the potential energy contribution between  $x$  and  $y$ , and  $y$  and  $x$  positions. The  $\epsilon_{\text{LiNbO}_3}$  is 4.821<sup>61</sup>. The calculated electrostatic potential energy for the two regions are shown in Figure 20(a) for the domain, and Figure 20(b) for the domain wall.

The electrostatic potential energy in the bulk domain from our calculations of polarization come out to be  $0.37\text{meV}$  in the bulk domain and  $0.45\text{meV}$  in the proximity of the domain wall. In contrast, the  $-T\Delta S$  at  $300\text{K}$  is  $-213\text{meV}$  at the bulk domain and  $-273\text{meV}$  in the proximity of the wall. Thus, the magnitudes are significantly different, and electrostatics would not prevent polar fluctuations.

#### Appendix H: Simulation of $\text{LiNbO}_3$ BF-STEM images

BF-STEM simulations of the  $\text{LiNbO}_3$  crystal structure were performed using the MacTempasX commercial software to understand the effect of tilt on imaging and atom position

Experimental Conditions	Value
Crystal Structure	$\text{LiNbO}_3$
Debye-Waller Parameters	$u_{\text{Li}} = 0.67\text{\AA}$
	$u_{\text{Nb}} = 0.3924\text{\AA}$
	$u_{\text{O}} = 0.5\text{\AA}$ <sup>48</sup>
Lattice Parameters	$a = 5.172\text{\AA}$
	$b = 5.172\text{\AA}$
	$c = 13.867\text{\AA}$ <sup>62</sup>
Space Group	161 (R3c) <sup>63</sup>
Zone Axis	$[1\bar{1}00]$
Accelerating Voltage	200kV
Inner Collection Angle	0mrad
Outer Collection Angle	15mrad
Cells	$1 \times 5$
Frozen Phonons	10
Slices per Unit Cell	5
Probe Semi-Angle	28mrad

TABLE IV. BF-STEM simulation conditions in MacTempasX

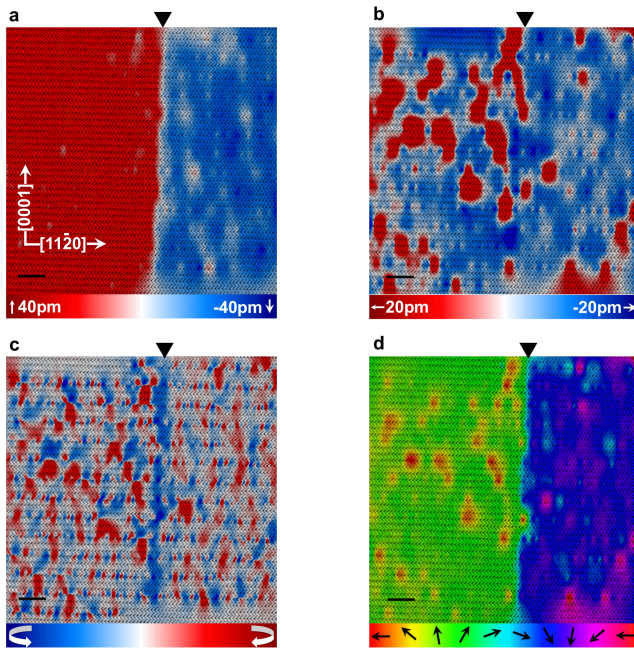


FIG. 15. Domain wall in Region 2. (a) Ising displacements at region 2 of the domain wall with non-equivalent polarization on either sides. (b) Néel displacements demonstrating the presence of strong alternating Néel components. (c) Curl of the polar niobium-oxygen displacement map with slight decrease at the domain wall. (d) Rotation map of the polar niobium-oxygen displacements. Scale bar in all images is 2nm.

metrology, with the simulation parameters being enumerated in Table IV, with the effect of increasing  $\alpha$  tilt being shown in Figure 21<sup>64</sup>. As could be observed, the relative distance being the niobium-oxygen columns is sensitive to tilt, with the distance decreasing with increasing tilt. However, since the average Niobium-Oxygen polar Ising displacements match extraordinarily closely with the theoretical values in the domain wall figures presented in this work, tilt is not a contributing factor. Additionally, while increasing tilt would result in closer niobium-oxygen columns in the up domain, as shown in Figure 21(c), it will also thus result in an increased distance in the down domain. However, the symmetric displacements observed (Figure 2, Figure 15, Figure 16, Figure 16, Figure 17, Figure 18) would indicate this is not in fact the case. Additionally, the effects of tilts should be global, with a constant increase or decrease in the displacement measured over the entire field of view. This is however not the case in any of the images presented, with the changes in the Ising or Néel displacements occurring over only a few unit cells. Considering that  $\text{LiNbO}_3$  is a brittle oxide, and a 30mrad tilt would result in enormous local stresses, it is safe to assume that it is local displacements rather than tilt which is being observed here.

\* alem@matse.psu.edu

- 1 J Willard Gibbs. On the equilibrium of heterogeneous substances. *American Journal of Science and Arts (1820-1879)*, 16(96):441, 1878.
- 2 Fred C Adams and Gregory Laughlin. A dying universe: the long-term fate and evolution of astrophysical objects. *Reviews of Modern Physics*, 69(2):337, 1997.
- 3 Enno Kätelhön, Stanislav V Sokolov, Thomas R Bartlett, and Richard G Compton. The role of entropy in nanoparticle agglomeration. *ChemPhysChem*, 18(1):51–54, 2017.
- 4 JJ Christensen, RM Izatt, LD Hansen, and JA Partridge. Entropy titration. a calorimetric method for the determination of  $\Delta G$ ,  $\Delta H$ , and  $\Delta S$  from a single thermometric titration1a, b. *The Journal of Physical Chemistry*, 70(6):2003–2010, 1966.
- 5 Karin M Rabe, Charles H Ahn, and Jean-Marc Triscone, editors. *Physics of Ferroelectrics: A Modern Perspective*. Springer, 2007.
- 6 Christopher T Nelson, Benjamin Winchester, Yi Zhang, Sung-Joo Kim, Alexander Melville, Carolina Adamo, Chad M Folkman, Seung-Hyub Baek, Chang-Beom Eom, Darrell G Schlom, et al. Spontaneous vortex nanodomain arrays at ferroelectric heterointerfaces. *Nano Letters*, 11(2):828–834, 2011.
- 7 Koji Kimoto, Toru Asaka, Xiuzhen Yu, Takuro Nagai, Yoshio Matsui, and Kazuo Ishizuka. Local crystal structure analysis with several picometer precision using scanning transmission electron microscopy. *Ultramicroscopy*, 110(7):778–782, 2010.
- 8 Sandra Van Aert, Stuart Turner, Rémi Delville, Dominique Schryvers, Gustaaf Van Tendeloo, and Ekhard KH Salje. Direct observation of ferrielectricity at ferroelastic domain boundaries

in  $\text{CaTiO}_3$  by electron microscopy. *Advanced Materials*, 24(4): 523–527, 2012.

- 9 Andrew B Yankovich, Benjamin Berkels, Wolfgang Dahmen, Peter Binev, Sergio I Sanchez, Steven A Bradley, Ao Li, Izabela Szlufarska, and Paul M Voyles. Picometre-precision analysis of scanning transmission electron microscopy images of platinum nanocatalysts. *Nature Communications*, 5:4155, 2014.
- 10 Benjamin H Savitzky, Ismail El Baggari, Alemayehu S Admasu, Jaewook Kim, Sang-Wook Cheong, Robert Hovden, and Lena F Kourkoutis. Bending and breaking of stripes in a charge ordered manganite. *Nature Communications*, 8(1):1883, 2017.
- 11 Malcolm E Lines and Alastair M Glass. *Principles and applications of ferroelectrics and related materials*. Oxford University Press, 1977.
- 12 Alexander Kirillovich Tagantsev, L Eric Cross, and Jan Fousek. *Domains in ferroic crystals and thin films*. Springer, 2010.
- 13 Gustau Catalan, J Seidel, R Ramesh, and James F Scott. Domain wall nanoelectronics. *Reviews of Modern Physics*, 84(1):119, 2012.
- 14 Venkatraman Gopalan, Volkmar Dierolf, and David A Scrymgeour. Defect–domain wall interactions in trigonal ferroelectrics. *Annual Review of Materials Research*, 37:449–489, 2007.
- 15 EA Eliseev, AN Morozovska, GS Svechnikov, Venkatraman Gopalan, and V Ya Shur. Static conductivity of charged domain walls in uniaxial ferroelectric semiconductors. *Physical Review B*, 83(23):235313, 2011.
- 16 Tomas Sluka, Alexander K Tagantsev, Petr Bednyakov, and Nava Setter. Free-electron gas at charged domain walls in insulating

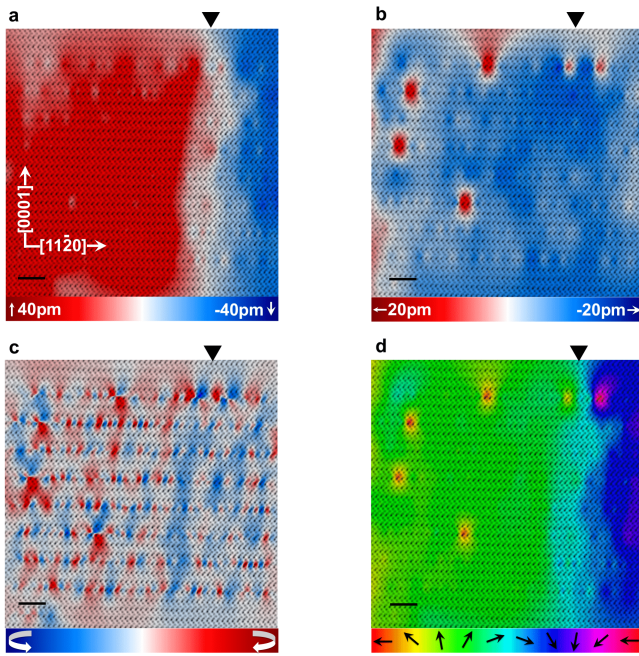


FIG. 16. Domain wall in Region 3. (a) Ising displacements at region 3 of the domain wall with non-equivalent polarization on either sides. (b) Néel displacements demonstrating the presence of consistent and uniform Néel components in contrast to region 2 (Figure 15). (c) Curl of the polar niobium-oxygen displacement map with a small discernible change at the domain wall. (d) Rotation map of the polar niobium-oxygen displacements. Scale bar in all images is 2nm.

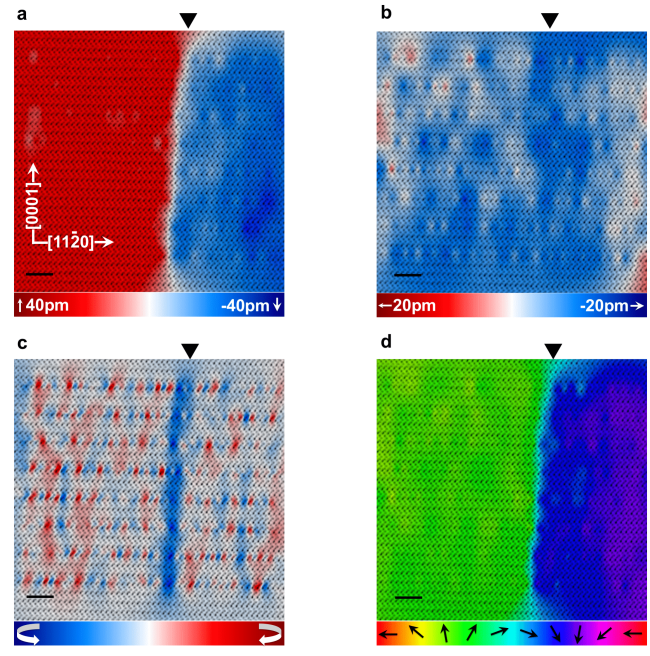


FIG. 17. Domain wall in Region 4. (a) Ising displacements at region 4 of the domain wall with non-equivalent polarization on either sides. (b) Néel displacements demonstrating the presence of Néel regions, not limited to only the domain wall. (c) Curl of the polar niobium-oxygen displacement map with a significant change only at the domain wall. (d) Rotation map of the polar niobium-oxygen displacements. Scale bar in all images is 2nm.

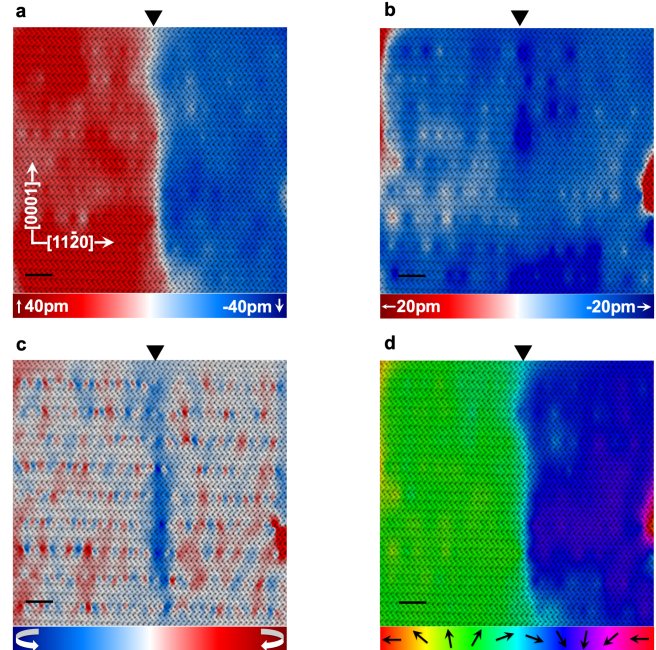


FIG. 18. Domain wall in Region 5. (a) Ising displacements at region 5 of the domain wall with a kink in the wall. (b) Quasi uniform Néel displacements in the proximity of the domain wall. (c) Curl of the polar niobium-oxygen displacement map. (d) Rotation map of the polar niobium-oxygen displacements, with the Ising kink being visible. Scale bar in all images is 2nm.

- BaTiO<sub>3</sub>. *Nature Communications*, 4:1808, 2013.
- <sup>17</sup> Donghwa Lee, Rakesh K Behera, Pingping Wu, Haixuan Xu, YL Li, Susan B Sinnott, Simon R Phillpot, LQ Chen, Venkatesan Gopalan, et al. Mixed Bloch-Néel-Ising character of 180° ferroelectric domain walls. *Physical Review B*, 80(6):060102, 2009.
  - <sup>18</sup> YJ Wang, D Chen, YL Tang, YL Zhu, and XL Ma. Origin of the Bloch-type polarization components at the 180° domain walls in ferroelectric PbTiO<sub>3</sub>. *Journal of Applied Physics*, 116(22): 224105, 2014.
  - <sup>19</sup> Xian-Kui Wei, Chun-Lin Jia, Tomas Sluka, Bi-Xia Wang, Zuo-Guang Ye, and Nava Setter. Néel-like domain walls in ferroelectric Pb(Zr, Ti)O<sub>3</sub> single crystals. *Nature Communications*, 7: 12385, 2016.
  - <sup>20</sup> Jacek C Wojdeł and Jorge Iniguez. Ferroelectric transitions at ferroelectric domain walls found from first principles. *Physical Review Letters*, 112(24):247603, 2014.
  - <sup>21</sup> Takao Matsumoto, Ryo Ishikawa, Tetsuya Tohei, Hideo Kimura, Qiwen Yao, Hongyang Zhao, Xiaolin Wang, Dapeng Chen, Zhenxiang Cheng, Naoya Shibata, et al. Multivariate statistical characterization of charged and uncharged domain walls in multiferroic hexagonal YMnO<sub>3</sub> single crystal visualized by a spherical aberration-corrected stem. *Nano Letters*, 13(10):4594–4601, 2013.
  - <sup>22</sup> Young-Min Kim, Stephen J Pennycook, and Albina Y Borisevich. Quantitative comparison of bright field and annular bright field imaging modes for characterization of oxygen octahedral tilts. *Ultramicroscopy*, 181:1–7, 2017.
  - <sup>23</sup> Qian He, Ryo Ishikawa, Andrew R Lupini, Liang Qiao, Eun J

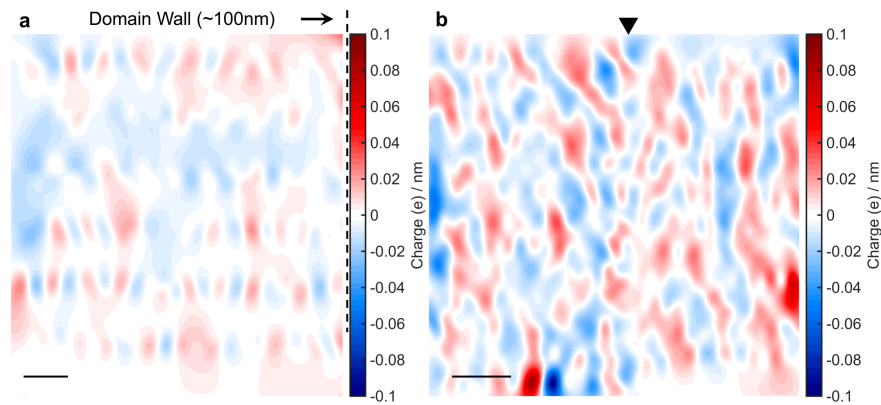


FIG. 19. Calculated charge accumulation. (a) Charge accumulation at a region of the bulk domain ( $\approx 100\text{nm}$ ) away from the wall. The polarization maps are given in Figure 13(a) and Figure 13(b) for the Ising and Néel displacements respectively (b) Charge accumulation in the proximity of the domain wall (Region 1), with the black triangle showing the domain wall location. The polarization maps are given in Figure 2(a) and Figure 2(b) for the Ising and Néel displacements respectively. Scale bar in both images is 2nm.

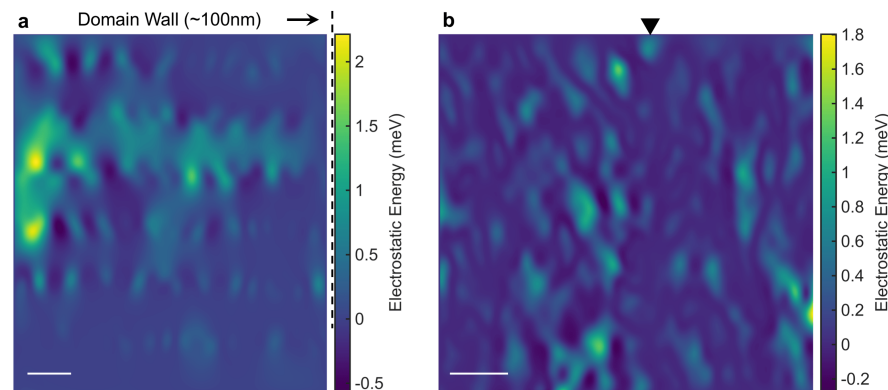


FIG. 20. Measured electrostatic potential energy. (a) Potential energy at a region of the bulk domain ( $\approx 100\text{nm}$ ) away from the wall. The polarization maps are given in Figure 13(a) and Figure 13(b) for the Ising and Néel displacements respectively (b) Potential energy in the proximity of the domain wall (Region 1), with the domain wall location shown by the black triangle. The polarization maps are given in Figure 2(a) and Figure 2(b) for the Ising and Néel displacements respectively. Scale bar in both images is 2nm. Potential energy was calculated with  $\epsilon_r = 4.821^{61}$ .

Moon, Oleg Ovchinnikov, Steven J May, Michael D Biegalski, and Albina Y Borisevich. Towards 3D mapping of  $\text{BO}_6$  octahedron rotations at perovskite heterointerfaces, unit cell by unit cell. *ACS Nano*, 9(8):8412–8419, 2015.

<sup>24</sup> T Malis, SC Cheng, and RF Egerton. EELS log-ratio technique for specimen-thickness measurement in the TEM. *Journal of Electron Microscopy Technique*, 8(2):193–200, 1988.

<sup>25</sup> Anubhav Jain, Shyue Ping Ong, Geoffroy Hautier, Wei Chen, William Davidson Richards, Stephen Dacek, Shreyas Cholia, Dan Gunter, David Skinner, Gerbrand Ceder, and Kristin A. Persson. The Materials Project: A materials genome approach to accelerating materials innovation. *APL Materials*, 1(1):011002, 2013. ISSN 2166532X.

<sup>26</sup> Julie Gonnissen, Dmitry Batuk, Guillaume F Nataf, Lewys Jones, Artem M Abakumov, Sandra Van Aert, Dominique Schryvers, and Ekhard KH Salje. Direct observation of ferroelectric domain walls in  $\text{LiNbO}_3$ : Wall-meanders, kinks, and local electric charges. *Advanced Functional Materials*, 26(42):7599–7604, 2016.

<sup>27</sup> David A Scrymgeour, Venkatraman Gopalan, Amit Itagi, Avadh Saxena, and Pieter J Swart. Phenomenological theory of a single domain wall in uniaxial trigonal ferroelectrics: Lithium niobate and lithium tantalate. *Physical Review B*, 71(18):184110, 2005.

<sup>28</sup> M Veithen and Ph Ghosez. First-principles study of the dielectric and dynamical properties of lithium niobate. *Physical Review B*, 65(21):214302, 2002.

<sup>29</sup> Jeffrey Goldstone. Field theories with «superconductor» solutions. *Il Nuovo Cimento (1955-1965)*, 19(1):154–164, 1961.

<sup>30</sup> Peter W Higgs. Broken symmetries and the masses of gauge bosons. *Physical Review Letters*, 13(16):508, 1964.

<sup>31</sup> Paško Županović and Domagoj Kulić. Relation between Boltzmann and Gibbs entropy and example with multinomial distribution. *Journal of Physics Communications*, 2(4):045002, 2018.

<sup>32</sup> Greg Stone, Colin Ophus, Turan Birol, Jim Ciston, Che-Hui Lee, Ke Wang, Craig J Fennie, Darrell G Schlom, Nasim Alem, and Venkatraman Gopalan. Atomic scale imaging of competing polar states in a Ruddlesden–Popper layered oxide. *Nature Communications*, 7:12572, 2016.

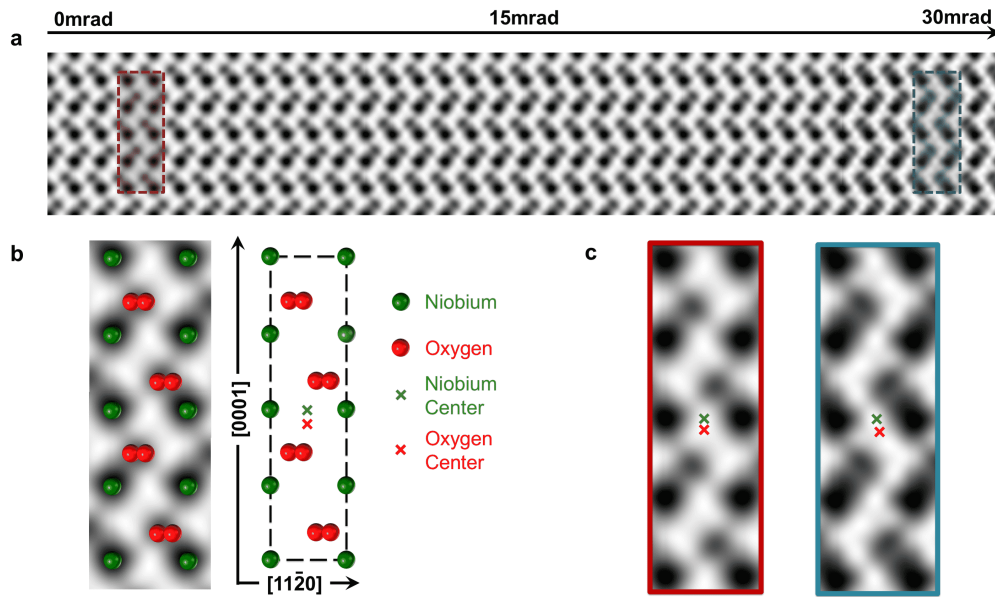


FIG. 21. Evolution of BF-STEM image as a function of  $\alpha$  tilt. (a) Multislice simulations of BF-STEM image of LiNbO<sub>3</sub> using the conditions detailed in Table IV without aberrations as a function of  $\alpha$  tilt from 0 mrad (no tilt) to 30 mrad of  $\alpha$  tilt. (b) Zoomed-in section with the niobium atoms in green and the oxygen atoms in red overlaid on top. (c) Comparison of the tilt effects at 0 mrad and 30 mrad showing how the relative displacement changes by 15pm in the  $[000\bar{1}]$  direction and by 25pm in the  $[11\bar{2}0]$  direction.

- <sup>33</sup> GA Smolenskii, NN Krainik, NP Khuchua, VV Zhdanova, and IE Mylnikova. The Curie Temperature of LiNbO<sub>3</sub>. *physica status solidi (b)*, 13(2):309–314, 1966.
- <sup>34</sup> Sungwon Kim, Venkatraman Gopalan, and Alexei Gruverman. Coercive fields in ferroelectrics: A case study in lithium niobate and lithium tantalate. *Applied Physics Letters*, 80(15):2740–2742, 2002.
- <sup>35</sup> HF Wang, YY Zhu, SN Zhu, and NB Ming. Investigation of ferroelectric coercive field in LiNbO<sub>3</sub>. *Applied Physics A: Materials Science & Processing*, 65(4):437–438, 1997.
- <sup>36</sup> Alessio Filippetti, Pietro Delugas, Maria Ilenia Saba, and Alessandro Mattoni. Entropy-suppressed ferroelectricity in hybrid lead-iodide perovskites. *The Journal of Physical Chemistry Letters*, 6(24):4909–4915, 2015.
- <sup>37</sup> R Piric, B Rožič, Z Kutnjak, R Blinc, Xinyu Li, and QM Zhang. Electrocaloric effect and dipolar entropy change in ferroelectric polymers. *Ferroelectrics*, 426(1):38–44, 2012.
- <sup>38</sup> Gian Giacomo Guzmán-Verri and Peter B Littlewood. Why is the electrocaloric effect so small in ferroelectrics? *APL Materials*, 4(6):064106, 2016.
- <sup>39</sup> Marcel Porta, Turab Lookman, and Avadh Saxena. Effects of criticality and disorder on piezoelectric properties of ferroelectrics. *Journal of Physics: Condensed Matter*, 22(34):345902, 2010.
- <sup>40</sup> Badari Narayana Rao, Ranjan Datta, S Selva Chandrashekar, Dileep K Mishra, Vasant Sathe, Anatoliy Senyshyn, and Rajeev Ranjan. Local structural disorder and its influence on the average global structure and polar properties in Na<sub>0.5</sub>Bi<sub>0.5</sub>TiO<sub>3</sub>. *Physical Review B*, 88(22):224103, 2013.
- <sup>41</sup> Miroslava Schaffer, Bernhard Schaffer, and Quentin Ramasse. Sample preparation for atomic-resolution STEM at low voltages by FIB. *Ultramicroscopy*, 114:62–71, 2012.
- <sup>42</sup> LA Giannuzzi. Reducing FIB damage using low energy ions. *Microscopy and Microanalysis*, 12(S02):1260–1261, 2006.
- <sup>43</sup> Joachim Mayer, Lucille A Giannuzzi, Takeo Kamino, and Joseph Michael. TEM sample preparation and FIB-induced damage. *MRS Bulletin*, 32(5):400–407, 2007.
- <sup>44</sup> Tim Grieb, Moritz Tewes, Marco Schowalter, Knut Müller-Caspary, Florian F Krause, Thorsten Mehrrens, Jean-Michel Hartmann, and Andreas Rosenauer. Quantitative HAADF STEM of SiGe in presence of amorphous surface layers from FIB preparation. *Ultramicroscopy*, 184:29–36, 2018.
- <sup>45</sup> Michael J Zachman, Zhengyuan Tu, Snehashis Choudhury, Lynden A Archer, and Lena F Kourkoutis. Cryo-STEM mapping of solid-liquid interfaces and dendrites in lithium-metal batteries. *Nature*, 560(7718):345, 2018.
- <sup>46</sup> Colin Ophus, Jim Ciston, and Chris T Nelson. Correcting nonlinear drift distortion of scanning probe and scanning transmission electron microscopies from image pairs with orthogonal scan directions. *Ultramicroscopy*, 162:1–9, 2016.
- <sup>47</sup> Oleg Tikhomirov, Hua Jiang, and Jeremy Levy. Local ferroelectricity in SrTiO<sub>3</sub> thin films. *Physical Review Letters*, 89(14):147601, 2002.
- <sup>48</sup> SC Abrahams, J Mi Reddy, and JL Bernstein. Ferroelectric lithium niobate. 3. single crystal x-ray diffraction study at 24°C. *Journal of Physics and Chemistry of Solids*, 27(6-7):997–1012, 1966.
- <sup>49</sup> William Hadley Richardson. Bayesian-based iterative method of image restoration. *Journal of the Optical Society of America*, 62(1):55–59, 1972.
- <sup>50</sup> Leon B Lucy. An iterative technique for the rectification of observed distributions. *The Astronomical Journal*, 79:745, 1974.
- <sup>51</sup> Xavier Gonze, François Jollet, F Abreu Araujo, Donat Adams, Bernard Amadon, Thomas Applencourt, Christophe Audouze, J-M Beuken, Jordan Bieder, A Bokhanchuk, et al. Recent developments in the ABINIT software package. *Computer Physics Communications*, 205:106–131, 2016.
- <sup>52</sup> Eberhard KU Gross and Reiner M Dreizler. *Density functional theory*, volume 337. Springer Science & Business Media, 2013.
- <sup>53</sup> Pierre Hohenberg and Walter Kohn. Inhomogeneous electron

- gas. *Physical Review*, 136(3B):B864, 1964.
- <sup>54</sup> Xavier Gonze, Bernard Amadon, P-M Anglade, J-M Beuken, François Bottin, Paul Boulanger, Fabien Bruneval, Damien Caliste, Razvan Caracas, Michel Côté, et al. ABINIT: First-principles approach to material and nanosystem properties. *Computer Physics Communications*, 180(12):2582–2615, 2009.
- <sup>55</sup> John P Perdew, Adrienn Ruzsinszky, Gábor I Csonka, Oleg A Vydrov, Gustavo E Scuseria, Lucian A Constantin, Xiaolan Zhou, and Kieron Burke. Restoring the density-gradient expansion for exchange in solids and surfaces. *Physical Review Letters*, 100(13):136406, 2008.
- <sup>56</sup> Miguel AL Marques, Micael JT Oliveira, and Tobias Burnus. Libxc: A library of exchange and correlation functionals for density functional theory. *Computer Physics Communications*, 183(10):2272–2281, 2012.
- <sup>57</sup> Michiel van Setten, Matteo Giantomassi, Eric Bousquet, Matthieu J Verstraete, Donald R Hamann, Xavier Gonze, and Gian-Marco Rignanese. The PseudoDojo: Training and grading a 85 element optimized norm-conserving pseudopotential table. *Computer Physics Communications*, 2018.
- <sup>58</sup> DR Hamann. Optimized norm-conserving Vanderbilt pseudopotentials. *Physical Review B*, 88(8):085117, 2013.
- <sup>59</sup> Fernando Casas, Ander Murua, and Mladen Nadinic. Efficient computation of the Zassenhaus formula. *Computer Physics Communications*, 183(11):2386–2391, 2012.
- <sup>60</sup> Hendrik J Monkhorst and James D Pack. Special points for brillouin-zone integrations. *Physical Review B*, 13(12):5188, 1976.
- <sup>61</sup> Izumi Tomeno and Sadao Matsumura. Elastic and dielectric properties of  $\text{LiNbO}_3$ . *Journal of the Physical Society of Japan*, 56(1):163–177, 1987.
- <sup>62</sup> H Boysen and F Altorfer. A neutron powder investigation of the high-temperature structure and phase transition in  $\text{LiNbO}_3$ . *Acta Crystallographica Section B: Structural Science*, 50(4):405–414, 1994.
- <sup>63</sup> Helen D Megaw. A note on the structure of lithium niobate,  $\text{LiNbO}_3$ . *Acta Crystallographica Section A: Crystal Physics, Diffraction, Theoretical and General Crystallography*, 24(6):583–588, 1968.
- <sup>64</sup> Michael A O’Keefe and Roar Kilaas. Advances in high-resolution image simulation. *Scanning Microscopy Supplement*, 2:225–244, 1988.